A high-frequency radio continuum study of massive young stellar objects

A.G. Gibb[1], M.G. Hoare[2]

[1]*Department of Physics and Astronomy, University of British Columbia, 6224 Agricultural Road, Vancouver, B.C. V6T 1Z1, Canada*
[2]*School of Physics and Astronomy, University of Leeds, Leeds, West Yorkshire, LS2 9JT*

ABSTRACT
We present high-resolution observations made with the Very Large Array (VLA) in its A configuration at frequencies between 5 and 43 GHz of a sample of five massive young stellar objects (YSOs): LkHα101, NGC2024-IRS2, S106-IR, W75N and S140-IRS1. The resolution varied from 0.04 arcsec (at 43 GHz) to 0.5 arcsec (at 5 GHz), corresponding to a linear resolution as high as 17 AU for our nearest source. A MERLIN observation of S106-IR at 23 GHz with 0.03-arcsec resolution is also presented. S106-IR and S140-IRS1 are elongated at 43 GHz perpendicular to their large scale bipolar outflows. This confirms the equatorial wind picture for these sources seen previously in MERLIN 5 GHz observations. The other sources are marginally resolved at 43 GHz. The spectral indices we derive for the sources in our sample range from +0.2 to +0.8, generally consistent with ionized stellar winds. We have modelled our sources as uniform, isothermal spherical winds, with LkHα101 and NGC 2024-IRS2 yielding the best fits. However, in all cases our fits give wind temperatures of only 2000 to 5000 K, much less than the effective temperatures of main-sequence stars of the same luminosity, a result which is likely due to the clumpy nature of the winds.

Key words: stars: formation – stars: winds, outflows – stars: early-type – radio continuum: stars

1 INTRODUCTION

Like their low-mass counterparts, young massive stars drive molecular outflows. The outflows from low-mass young stellar objects (YSOs) appear to be driven by highly-collimated jets emanating from the central star-disc region (e.g., Reipurth et al. 2002; Burrows et al. 1996; Ouyed, Clarke & Pudritz 2003). The situation for massive YSOs is less clear: only in a small number of cases have jets been detected, and those detections have all been at centimetre wavelengths (e.g., HH 80–81 – Martí et al. 1993; Cep A-HW2 – Rodríguez et al. 1994; W3-H_2O – Wilner, Reid & Menten 1999; and G35.2−0.7N – Gibb et al. 2003). Surprisingly, *equatorially*-elongated radio emission has been detected towards three sources: S 106 (Hoare et al. 1994), S 140-IRS1 (Hoare 2006) and more recently Orion-I (Reid et al. 2007). Hoare (2002) summarizes the radio properties of massive YSOs.

The primary mechanism for the radio continuum emission from massive YSOs is thermal free-free emission from ionized gas. This may either be in the form of a photo-ionized H II region or stellar wind. An infinite, constant velocity ionized wind has a spectral index of +0.6 (Wright & Barlow 1975; Panagia & Felli 1975), while that for an H II region varies from −0.1 (optically thin) to +2 (optically thick). However, if the wind is finite in extent (i.e. the ionized gas recombines to form a neutral wind), then the spectral index can increase as the wind begins to take on the appearance of an optically thick H II region (Simon et al. 1983; Moran et al. 1983). For

collimated flows, the spectral index (for unresolved sources) can take on values between 0.25 and 1.1, although a conical flow yields the same spectral index as expected for a spherical wind (Reynolds 1986).

Infrared recombination line studies have shown that the winds from massive YSOs can reach speeds of several hundred $km\,s^{-1}$ (Drew, Bunn & Hoare 1993; Bunn, Hoare & Drew 1995). However, these spectral studies are not able to resolve the geometry of the high-velocity gas. For this we must turn to the radio to achieve the high spatial resolution necessary to probe the small-scale structure of the ionized gas.

Although theoretically attractive, it remains unclear whether a circumstellar disc forms during the collapse of a massive cloud core and if so whether it survives the pre-main sequence evolution of a massive YSO given the detrimental impact of the wind and ionizing radiation (e.g. Richling & Yorke 1997). The observation of jet-like outflows suggests that discs do indeed form in some cases, while recent high-resolution submillimetre imaging has yielded good observational evidence for a disc around a massive YSO (Patel et al. 2005).

In this paper we present the results of a high-resolution, multi-wavelength radio survey of a sample of five massive YSOs (Table 1), none of which has evidence for a jet. Furthermore, none of these have been previously observed at 43 GHz, nor with such high angular resolution. Previous 43 GHz studies of high-mass YSOs have

Table 1. Source properties. Coordinates are of the phase centres used in the observations. The notation $a(b)$ represents $a \times 10^b$.

Source	RA (B1950)	Dec (B1950)	d (kpc)	L ($L_\odot$)
S 106-IR	20:25:33.8	+37:12:49.98	0.6	2.0(4)
S 140-IRS1	22:17:41.1	+63:03:41.58	0.9	5.0(3)
W75N	20:36:50.0	+42:26:57.13	2.0	4.4(4)
NGC 2024-IRS2	05:39:14.3	−01:55:55.00	0.42	1.0(4)
Lk Hα101	04:26:57.2	+35:09:54.95	0.7	4.0(4)

Table 2. Coordinates of detected sources.

Source	RA(B1950)	Dec(B1950)	ID
S 106-IR	20:25:33.823	+37:12:50.04	IR/IRS4
S 140-IRS1	22:17:41.085	+63:03:41.58	IRS1
	22:17:41.051	+63:03:59.41	IRS2N
W75N	20:36:50.005	+42:26:58.49	VLA1/Ba
	20:36:50.042	+42:26:57.13	VLA3/Bb
	20:36:50.084	+42:26:55.46	Bc
NGC 2024-IRS2	05:39:14.301	−01:55:55.00	IRS2
Lk Hα101	04:26:57.235	+35:09:54.95	LkHα101

been published by Menten & van der Tak (2004), van der Tak & Menten (2005) and van der Tak, Tuthill, & Danchi (2005), and these are discussed later. Menten & Reid (1995) and Rodríguez et al. (2005) present 43-GHz observations of BN and Orion-I, although these papers do not discuss the physical properties derived from these data. The high-frequency radio continuum spectra of these sources are discussed by Plambeck et al. (1995). The aims of the current study were to explore the high-frequency characteristics via the spectral index (for clues to emission mechanisms) and small-scale geometry of the ionized winds from massive YSOs. This paper presents the results of these observations, and provides new information on the geometry of the ionized gas close to these massive YSOs.

2 OBSERVATIONS

The observations were made using the Very Large Array (VLA) of the National Radio Astronomy Observatory in its most extended (A) configuration. The data were recorded on 1996 November 1. Each of the sources listed in Table 1 was observed at C (4.86 GHz), X (8.46 GHz), K (22.46 GHz) and Q (43.49 GHz) band. At the time of observation, the VLA had 43-GHz receivers on 13 antennas, leaving 14 to be used at other frequencies (although only 12 were useable). Our observing procedure was to observe the source for the full on-source time with the Q-band subarray and split the observing time for the non-Q band subarray between the other three frequencies. The typical on-source time was 9 minutes at 5 GHz, 9 minutes at 8.5 GHz, 7 to 15 minutes at 22.5 GHz and 30 minutes at 43 GHz.

The minimum and maximum telescope separations at each frequency was 1.6 to 25.6 km (C, X and K), and 1.0 to 34.6 km (Q). The resolution at each of these frequencies ranges from 0.4 arcsec (C band) to 35 milliarcsec (Q band). At the distance of our closest source (NGC 2024-IRS2) the resolution at 43 GHz corresponds to ∼17 AU, and 85 AU for our most distant source (W75N).

Absolute amplitude calibration was carried out using 0134+329 (C, X and K band) and 0710+439 (Q band). Calibrator details are given in Table 3, where the names are given in B1950 form. A model was used for 0134+329 at K band. Although

0134+329 is a VLA standard calibrator, it could not be used at 43 GHz due to limitations in the number of antennas near the centre of the array in this subarray. Therefore, the flux of 0710+439 has been assumed based on previous observations. A correction for atmospheric opacity was made at 43 GHz, as tipping scans yielded a zenith optical depth of 0.1. The estimated calibration uncertainty is less than one per cent at 5, 8.5 and 22.5 GHz. At 43 GHz the absolute uncertainty is much higher at ∼30 per cent, although the relative uncertainty is small, typically less than 5 per cent.

Nearby quasars were used for phase referencing (denoted by 'P' in Table 3). The 'fast-switching' technique was employed at 43 GHz, in order to limit decorrelation due to atmospheric phase fluctuations, with a cycle time of approximately 2 minutes (Carilli & Holdaway 1999). The bootstrapped flux densities of the phase calibrators are generally self-consistent, although the K-band flux for 2023+336 appears to be anomalously low.

The data were edited and calibrated using the AIPS package, and reduced and analyzed using AIPS and MIRIAD (Sault et al. 1995). Images were constructed using a variety of weighting schemes by varying the Briggs robust parameter. In general, a neutral value of 0 gave the optimum balance between resolution and sensitivity to any extended emission. Table 4 lists the beam parameters and sensitivity for each source at each wavelength.

2.1 Additional observations

We also observed S106-IR at 23 GHz with MERLIN on 1996 May 5. 3C273 was used for pointing and absolute calibration, assuming a flux density of 20 Jy. 2023+335 was used for phase calibration. In order to obtain a reasonable image, a 15 Mλ taper was applied to the data to give a beam of 0.031×0.028 arcsec^2 and a noise level of 0.95 mJy beam^{-1}. Only four of the MERLIN antennas were used so the image fidelity is poor. However, the general size and shape of the emission are robust.

S106-IR and NGC2024-IRS2 were also observed at 86 and 106 GHz with the Plateau de Bure interferometer (PdBI) on several dates during 1996 September and October with the antennas in the C and D configurations. The data were calibrated using the CLIC software package. NRAO 150 was used for bandpass calibration, 0458−020 and 2013+370 for phase calibration. The amplitude calibration was derived by a bootstrap method, solving iteratively for the antenna gains. The beamsize was ∼4–4.5 arcsec and noise level was 10–20 mJy beam^{-1}. Fluxes were derived from Gaussian fits to the visibility data. S106-IR was not detected (although extended emission was detected; see Bieging 1984); NGC2024-IRS2 was detected as a point source with a flux density of 60/110 mJy at 86/106 GHz respectively.

3 RESULTS & ANALYSIS

In this section we introduce each source, present images at each frequency and calculate spectral indices. Visibility amplitude plots are shown in section 4.1. Source positions were derived from 2-D gaussian fits at each wavelength and found to be consistent at all wavelengths to within 0.04 to 0.06 arcsec, in good agreement with the expected accuracy stated in the VLA Observational Status Summary. The position of each detected source is listed in Table 2.

Flux estimates for each source were derived in two ways. The first was to sum the emission within a region encompassing the source, and the second was to carry out a two-dimensional gaussian fit. In most cases, the sources were well-fit by gaussians and the

Table 3. Calibrator properties. Amplitude calibrators are denoted by an 'A' in the Calibrator Type column. The Notes column denotes how the flux was obtained: 'D' – derived within AIPS, 'A' – assumed, 'B' – bootstrapped from amplitude calibrator. Fluxes for 0134+329 (at 5 and 8.5 GHz) and 0316+329 (at 22.5 GHz) were derived using standard VLA calibration procedures within AIPS. Fluxes for the phase calibrators (denoted by a 'P' in the Calibrator Type column) are bootstrapped values derived from the amplitude calibrators. Note that the uncertainties in the bootstrapped 43-GHz fluxes does not include the uncertainty in the absolute calibration.

Calibrator	Flux density (Jy)				Calibrator Type	Notes
	5 GHz	8.5 GHz	22.5 GHz	43 GHz		
0134+329	5.51 ± 0.03	3.22 ± 0.01	1.12 ± 0.01	–	A	D
0710+439	–	–	–	0.3 ± 0.1	A	A
0440+345	1.00 ± 0.01	0.83 ± 0.02	0.34 ± 0.02	–	P	B
0441+341	–	–	–	0.52 ± 0.01	P	B
0539−057	0.95 ± 0.02	1.00 ± 0.03	0.76 ± 0.04	0.46 ± 0.02	P	B
2005+403	–	–	–	1.09 ± 0.03	P	B
2023+336	2.80 ± 0.03	2.60 ± 0.06	1.72 ± 0.05	2.56 ± 0.08	P	B
2229+695	0.37 ± 0.01	0.40 ± 0.01	0.39 ± 0.02	0.31 ± 0.01	P	B

Table 4. Observational parameters. The noise level (1σ in mJy beam^{-1}) and beam dimensions (in arcsec) are those of the maps presented in this paper. The number in parentheses after the beam dimensions is the beam position angle, measured in degrees east of north.

Source	5 GHz		8.5 GHz		22.5 GHz		43 GHz	
	Noise	Beam	Noise	Beam	Noise	Beam	Noise	Beam
S 106-IR	—	—	0.064	$0.26\times0.19\,(-23)$	0.25	$0.100\times0.069\,(+6)$	0.35	$0.040\times0.031\,(-69)$
S 140-IRS1	0.041	$0.55\times0.31\,(-27)$	0.034	$0.32\times0.18\,(-23)$	0.28	$0.120\times0.071\,(-7)$	0.36	$0.042\times0.031\,(-45)$
W75N	0.048	$0.50\times0.33\,(-35)$	0.034	$0.29\times0.19\,(-32)$	0.32	$0.106\times0.077\,(-4)$	0.30	$0.041\times0.031\,(-63)$
NGC 2024-IRS2	0.200	$0.67\times0.51\,(-34)$	0.091	$0.43\times0.30\,(-43)$	0.47	$0.138\times0.102\,(+83)$	0.40	$0.063\times0.039\,(-42)$
Lk Hα101	0.043	$0.55\times0.36\,(+61)$	0.055	$0.33\times0.22\,(+67)$	0.30	$0.129\times0.069\,(+72)$	0.31	$0.041\times0.034\,(-89)$

dimensions listed for each source are the deconvolved major and minor axes derived from these fits (Tables 5 and 6). Any significant deviations from a gaussian fit are discussed in the text. Gaussian fits to the visibility data gave poor results, significantly over-estimating the total flux and were therefore not used in our analysis. The uncertainties in the peak and total fluxes given in Table 5 represent the mean residual between the source and a gaussian fit, and do not include contributions from the uncertainty in the absolute calibration. Brightness temperatures were derived from the peak fluxes using the beam sizes given in Table 4. These will be lower limits to the actual temperature of the gas due to low optical depth and/or incomplete beam filling.

The centimetre spectral energy distribution for each source was fitted between 5 and 43 GHz to derive a spectral index (also listed in Table 5). In addition we calculated the index for the angular size as a function of frequency, which we denote by ζ (and list in Table 6). We also plot 3-mm fluxes on the spectral energy distribution for comparison.

3.1 S106-IR

S106 is a well-known optical and radio bipolar H II region (Bally, Snell & Predmore 1983; Bally et al. 1998). Bally et al. (1983) detected a compact radio source at the centre of the H II region co-incident with the infrared source S106-IR (also known as IRS4). Mid-infrared imaging by Smith et al. (2001) show that S106-IR is the sole exciting source of the large-scale ionized nebula. Infrared spectroscopy by Drew, Bunn & Hoare (1993) revealed the presence of a highly supersonic, ionized wind with a terminal velocity exceeding 340 km s^{-1} and inferred that enhanced mass-loss must be occurring along the equatorial direction. High-resolution radio observations at 5 GHz with MERLIN revealed the ionized gas takes on an equatorial configuration in the radio with a position angle

of -61 ± 2 degrees (Hoare et al. 1994). The X-ray results of Giardino et al. (2004) are consistent with shocks in a radiatively-driven stellar wind. Near-infrared speckle observations by Alvarez et al. (2004) show only a single unresolved source.

We observed S106-IR at 8.5, 22.5 and 43 GHz (Fig. 1). In addition we present MERLIN 23-GHz data for comparison in Fig. 1d (see also Hoare & Muxlow 1996). Contamination from the large-scale H II region was a significant problem at 8.5 GHz; we only include data on baselines greater than 200 kλ in Fig. 1a. Compact emission was detected only from S106-IR; the nearby protostellar source S106-FIR was not detected to a 3-σ limit of 0.15 mJy at 8.5 GHz and 1.1 mJy at 43 GHz.

S106-IR is marginally resolved at 22.5 GHz, and is clearly resolved (along the long axis) at 43 GHz showing an elongated geometry a direction perpendicular to the large-scale H II region. The 5-GHz MERLIN observations of Hoare et al. (1994) revealed a source elongated perpendicular to the direction of the large-scale bipolar H II region. Our results show that the emission at 43 GHz has a similar geometry, reinforcing the interpretation of Hoare et al. (1994) that the ionized gas is confined to an equatorial configuration. The MERLIN map at 23 GHz (Fig. 1d) coupled with the fact that there is no known outflow with this position angle confirms the equatorial geometry beyond doubt.

The gaussian fit to the 22.5-GHz VLA image in Fig. 1b (made with a robust parameter of -2) yields a point source upon deconvolution. However, we note that there is a slight east-west elongation in the lower contours for this image. The fit to an image made with a robust parameter of $+2$ yields an east-west deconvolved source geometry: 0.057×0.013 arcsec^2 at a position angle of -87 degrees. This is in reasonable agreement with the fit to the MERLIN 23-GHz data which gives 0.074×0.03 arcsec^2 at a position angle of -63 degrees. The VLA 43-GHz data are in excellent agreement with the MERLIN data, showing a position angle of -61 degrees.
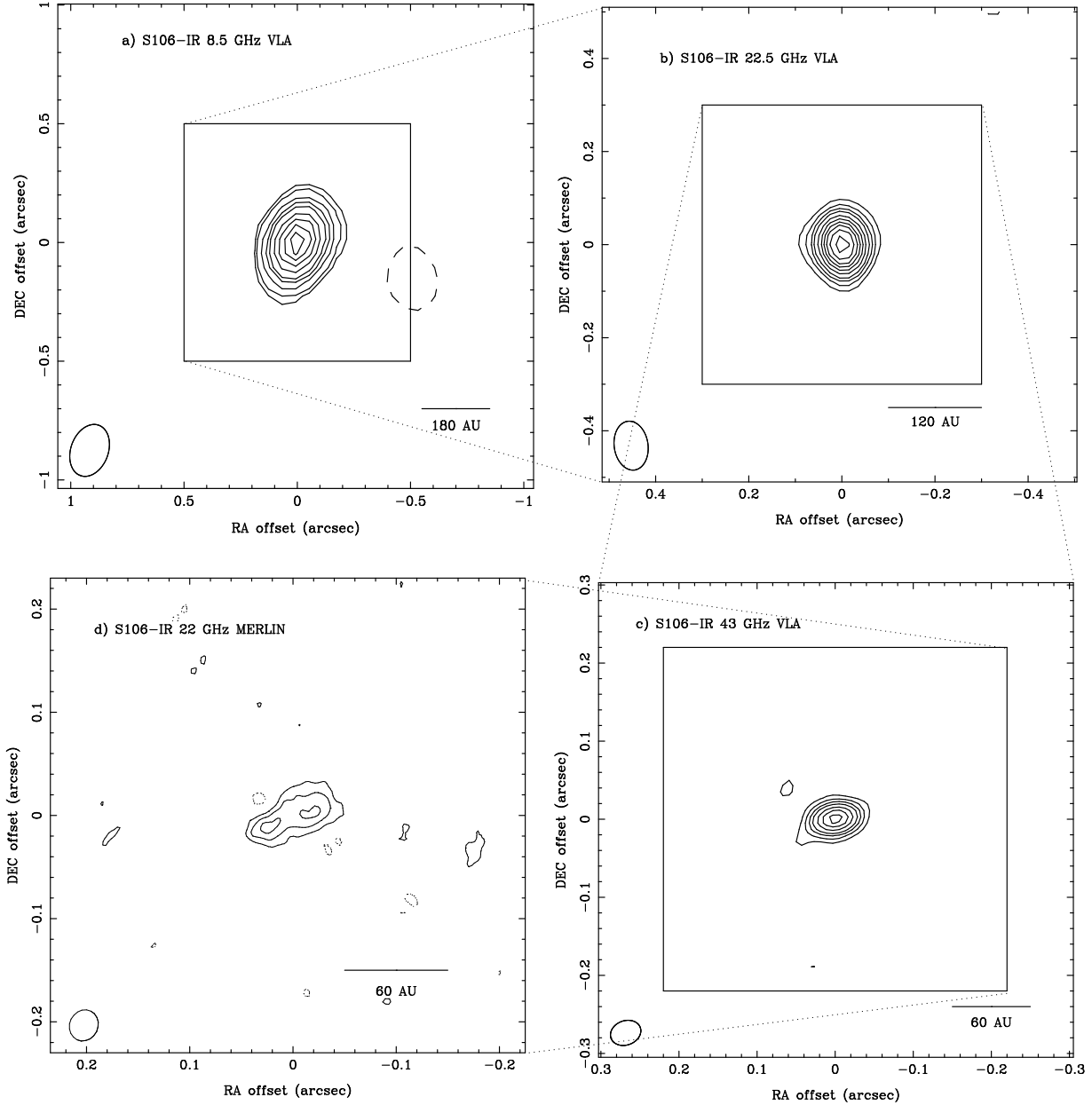
Figure 1. Images of S106-IR at each frequency, clockwise from top left: a) 8.5 GHz, b) 22.5 GHz, c) 43 GHz and d) 22 GHz MERLIN data. Contours are at a) $-3, 3, 5, 10, 15, 20, 30, 40, 50, 60 \times 0.064$ mJy beam^{-1}; b) $-3, 3, 5, 7, 9, 12, 15, 18, 21, 25, 30, 35 \times 0.25$ mJy beam^{-1}; c) $-3, 3, 5, 7, 9, 12, 15, 18 \times 0.35$ mJy beam^{-1}; and d) $-1, 1, 2, 3 \times 1.5$ mJy beam^{-1} respectively. The large box in a), b) and c) represents the size of the next image. The open ellipse in the bottom left corner represents the beam, and a scale bar is shown as a horizontal line assuming the distance given in Table 1. The coordinates for the MERLIN image given by Hoare & Muxlow (1996) were corrected for the different epoch used at the VLA.

The VLA 22.5-GHz flux measurement is in good agreement with MERLIN measurement within the uncertainties. Both measurements are slightly lower than the 17 mJy measured by Felli et al. (1984). We see no evidence of the double-peaked appearance in our VLA observations compared with the MERLIN data but our highest VLA resolution ($\sim$0.035 arcsec at 43 GHz) is barely sufficient to resolve these maxima.

We derive a spectral index of $+0.65\pm0.11$ from the VLA data, in good agreement with the value of 0.7 derived by Bally et al. (1983). However, we note that our fluxes are consistently lower by $\sim$60 per cent, which is probably a result of our observations being less sensitive to extended emission than previous. The angular-size

as a function of frequency for the VLA data is flatter than expected for a uniform spherical wind, but only two points contribute to this fit. The higher-resolution MERLIN data (although also only two points) give a value for ζ of -0.59, very close to the value predicted for a uniform wind. Based on the MERLIN results of Hoare et al. (1994) and the data presented here, the predicted source diameter at 43 GHz is $\sim$0.05 arcsec, a little larger than our derived value of 0.031 arcsec.

The brightness temperature increases with frequency, indicating that the higher-frequency observations are tracing hotter gas close to the star. However, the brightness temperatures derived from the VLA data are all considerably lower than either the likely equiv-
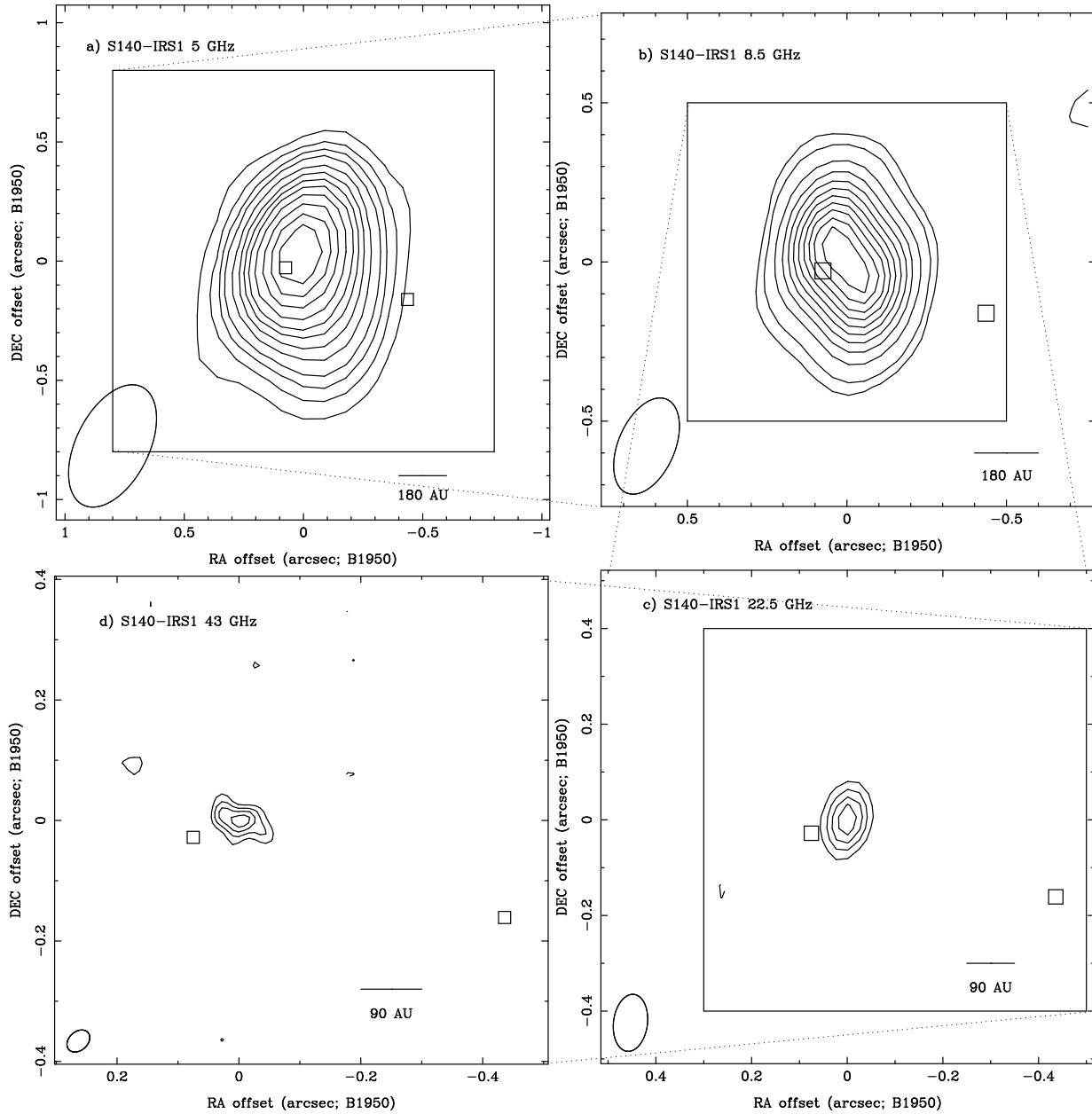
Figure 2. Images of S140-IRS1 at each frequency, clockwise starting from top left: a) 5 GHz, b) 8.5 GHz, c) 22.5 GHz and d) 43 GHz. Open squares are water masers from Tofani et al. (1995). Contours are at: a) -3, 3, 5, 7, 9, 12, 15, 18, 21, 25, 30, 35, 40×0.041 mJy beam^{-1}; b) -3, 3, 5, 10, 15, 20, 25, 30, 35, 40, 45, 50, 55, 60, 65, 70, 75, 80×0.034 mJy beam^{-1}; c) -3, 3, 5, 7, 9, 12, 15×0.28 mJy beam^{-1} and d) -3, 3, 5, 7, 9, 12×0.36 mJy beam^{-1} respectively. The large box in a), b) and c) represents the size of the next image. The open ellipse in the bottom left corner represents the beam, and a scale bar is shown as a horizontal line assuming the distance given in Table 1.

alent main-sequence effective temperature of 22 000 K or even half that value (see Drew 1989). Comparing these values with those derived from the MERLIN data (18 000 and 13 500 K at 5 and 23 GHz respectively) suggests that the emission is clumpy and has structure on scales smaller than the VLA beam.

3.2 S140-IRS1

S140-IRS1 is the brightest of a group of infrared sources and has long been known to be associated with radio emission and a bipolar CO outflow (Simon et al. 1983; Schwartz 1989; Minchin, White & Padman 1993b). A compact near-infrared reflection nebula is ob-

served in the direction of the blue lobe of the CO outflow (Hoare, Glindemann & Richichi 1996; Schertl et al. 2000; Alvarez et al. 2004). IRS1 is also associated with water masers (Tofani et al. 1995) and its radio emission is elongated perpendicular to the reflection nebula and outflow directions (Hoare 2006). Thus S 140-IRS1 is a second example of a massive YSO with an equatorial wind.

S140-IRS1 was observed at all four frequencies in our survey (Fig 2). IRS1 is clearly detected and is resolved at 5, 8.5 and 43 GHz; only at 22.5 GHz does it appear to be a point source, probably due to a lack of sensitivity. The 43-GHz emission is especially interesting as we clearly resolve structure in the ionized gas

on scales of 40 AU. The emission is elongated in a similar direction to that seen previously at lower frequencies (Schwartz 1989; Tofani et al. 1995; Hoare 2006). The position angle (PA) of the extended arms is ∼60–65 degrees east of north, compared with 35 degrees for the 5 and 8.5-GHz emission. A line drawn through the tips of the extended emission defines a PA of ∼45 degrees. The MERLIN 5-GHz observations shown by Hoare (2006) have a very similar PA of ∼45 degrees, although that emission is more extended than our 43-GHz data. However, unlike the 5-GHz MERLIN data, which shows linearly extended emission, the 43-GHz image displays a clockwise twist in the lower contours, which gives the appearance of anti-clockwise rotation (Hoare 2006). Furthermore, the proper motion of the ionized gas is consistent with the rotation interpretation (Hoare 2006). There is good agreement between our 8.5-GHz image (Fig. 2b) and that of Tofani et al. (1995), showing the same twist in the lower contours.

The spectral index of IRS1 is well-constrained and consistent with a constant velocity ionized wind ($\alpha = 0.61\pm0.03$). Furthermore, the deconvolved size of the emission from IRS1 falls off in a manner close to that expected for a uniform spherical wind. Previous estimates of the spectral index give a slightly higher value of 0.8 (Schwartz 1989; Tofani et al. 1995) for the central source and a smaller value for the extended emission (interpreted as a jet by Schwartz 1989). The brightness temperatures at 5 and 8.5 GHz are rather similar at a little less than 600 K (Table 5). They increase at 22.5 and 43 GHz but remain below 2000 K. Extrapolating to higher frequencies shows that the wind from IRS1 contributes a significant fraction of the flux at 3 mm (Fig. 6).

The 5-GHz MERLIN data of Hoare & Muxlow (1996) and Hoare (2006) reveal a more elongated source which is somewhat larger than predicted by the value for ζ given in Table 6. This may be a result of our observations not detecting all of the emission. An intriguing fact is that the 43-GHz data has a different position angle to the MERLIN data, although it must be noted that the extent of the 43-GHz emission lies within the central part of the MERLIN image.

We also detected IRS2N at 5 and 8.5 GHz, with a spectral index of ∼0.77, in reasonable agreement with previous determination by Schwartz (1989), at least for the 1.6 and 5 GHz data. It is likely that IRS2N is an HII region, with a turnover frequency below 15 GHz (c.f. Schwartz 1989), and is optically thin and resolved at 22.5 and 43 GHz.

IRS2S was not detected above a 3-σ level of 0.1 mJy beam^{-1} at 8.5 GHz, despite its clear detection with a flux density of ∼1 mJy at 5 and 8.4 GHz by Schwartz (1989) and Tofani et al. (1995) respectively. IRS3 was not detected to the same levels.

IRS2S was detected by Tofani et al. (1995) at 8.5 GHz with a flux density of 1.2 mJy beam^{-1} in 1992 November, compared with our 3σ upper limit of 0.1 mJy beam^{-1} in 1996 November, a reduction of more than an order of magnitude over a 4-year timescale. Tofani et al. (1995) derived a spectral index for IRS2S of 0.6 (between 1.5 and 8.5 GHz), as expected for a constant velocity wind. Therefore, IRS2S is an embedded massive YSO driving an ionized wind. Our non-detection may be due to resolving out of the emission, but we note that the observations by Tofani et al. (1995) also used the VLA in A-configuration. Therefore it is more likely that IRS2S is variable at centimetre wavelengths.

The 'bullet' source (VLA4 in Simon et al. 1983) was not detected in any of our images despite having sufficient sensitivity to detect it. It is therefore likely (and perhaps suggested by previous images) that this source is extended and is resolved out by our observations.

No radio emission was detected towards the location of the submillimetre source SMM1 (Minchin, Ward-Thompson & White 1993a) to a 3-σ limit of 1.1 mJy at 43 GHz (0.1 mJy beam^{-1} at 8.5 GHz).

3.3 W75N

W75N contains a small cluster of radio sources associated with a group of water masers (Hunter et al. 1994). A large-scale CO outflow is observed orientated in a predominantly east-west direction (Davis et al. 1998), although higher-resolution studies have shown that the flow is composed of several overlapping outflows from a small cluster of YSOs (Shepherd, Testi, & Stark 2003). The main group of radio sources lie within a region approximately 3 arcsec in diameter and lie in a north-south arrangement. Hunter et al. (1994) resolved 3 sources, while observations at 22 GHz resolved four (VLA1–4: Torrelles et al. 1997). VLA1 has a jet-like appearance with the same position angle as the larger scale CO outflow seen by Davis et al. (1998). Shepherd (2001) detected a compact dust source coincident with the group of radio sources peaking on VLA3 (= W75N Bb in the nomenclature of Hunter et al. 1994).

We imaged W75N at all four wavelengths (Fig. 3). At 5 and 8.5 GHz we detect the three sources which make up W75N B (Hunter et al. 1994). At 22.5 and 43 GHz we only detect the most deeply embedded source VLA3 (W75N Bb). The 43-GHz flux density of VLA3 may be as much as 50 per cent higher since images made with natural weighting recover a larger flux. However, we note that Shepherd, Kurtz & Testi (2004) report a similar value to that we measure from our image (5.7 mJy compared with 5.2 mJy). From a gaussian fit, VLA3 appears to be resolved at 43 GHz: its appearance in Fig. 3d is circular despite the elongated beam. It is interesting to note that the position angle of the 43-GHz emission (due north) is almost perpendicular to the proposed outflow direction (PA of 101 deg) from Shepherd et al. (2003). However, it is also vastly different to the position angle of the 22-GHz emission imaged by Torrelles et al. (1997), although our source size is in good agreement with theirs. Clearly, further high-resolution observations are desirable to constrain the small-scale geometry of this source.

We do not detect the source VLA2 at any wavelength, probably for a combination of it being too faint (its flux density at 22.5 GHz is only ∼4 times our noise level: Torrelles et al. 1997) and too extended for our observations (Shepherd et al. 2004 detect it with a larger beam at 43 GHz with a similar sensitivity to ours). VLA1 is too weak for us to detect at 22.5 GHz: its peak flux density is roughly at our 4-σ level (Torrelles et al. 1997).

We derive a spectral index of 0.79$\pm$0.15 for VLA3, although the fit is rather poor: from Fig. 6 it is clear that the observed fluxes do not lie on a straight line. However, our spectral index is consistent with an ionized wind and the value of 0.5 derived by Shepherd et al. (2004) at the 2-σ level. The spectral index derived by Torrelles et al. (1997) is higher at +1.5, although their estimate comes from non-simultaneous observations. The brightness temperature of VLA3 increases with frequency, although it is much lower than the typical temperature of ionized gas and the stellar effective temperature.

Our spectral index for W75N-Bc is in excellent agreement with that derived by Shepherd et al. (2004). These authors point out that it is likely that Bc has significant extended flux, which we are filtering out in our high-resolution observations. The biggest difference lies with the spectral index for VLA1, for which we calculate a large negative value, compared with previous positive estimates
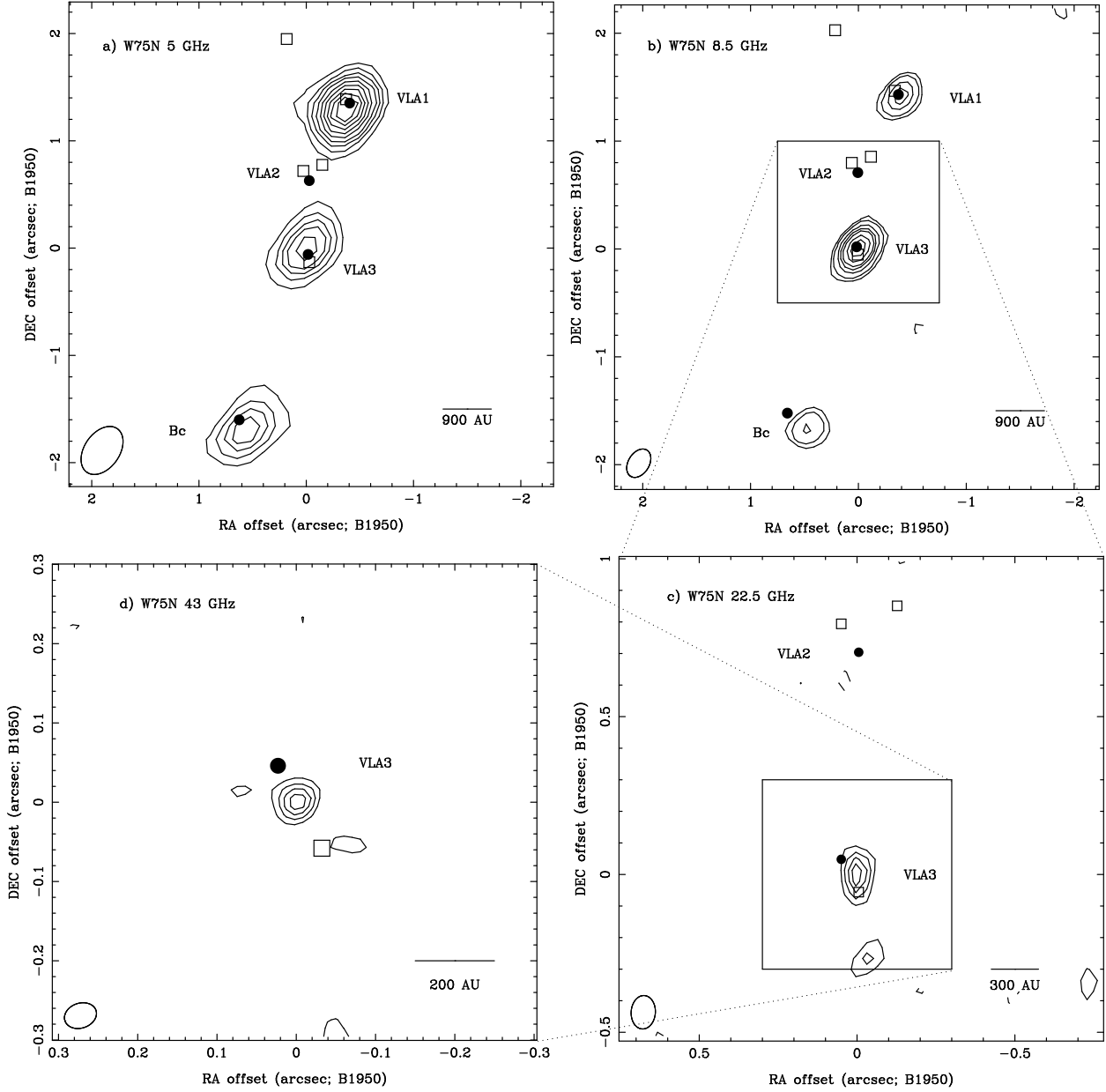
Figure 3. Images of W75N at each frequency, clockwise starting from top left: a) 5 GHz, b) 8.5 GHz, c) 22.5 GHz and d) 43 GHz. Open squares are water masers from Hunter et al. (1994) and filled circles are radio positions from Hunter et al. and Torrelles et al. (1997). Contours are at: a) -3, 3, 5, 7, 9, 12, 15, 18, 21, 24$\times$0.048 mJy beam^{-1}; b) -3, 3, 5, 10, 15, 20, 30, 40, 40$\times$0.034 mJy beam^{-1}; c) -3, 3, 5, 7, 9$\times$0.32 mJy beam^{-1} and d) -3, 3, 5, 7, 9$\times$0.3 mJy beam^{-1} respectively. The large box in the b) and c) represents the size of the next image. The open ellipse in the bottom left corner represents the beam, and a scale bar is shown as a horizontal line assuming the distance given in Table 1.

of 0.2 to 0.7. This is undoubtedly a consequence of our resolving out of emission at 8.5 GHz compared with the lower-resolution observations of Hunter et al. (1994).

3.4 NGC2024-IRS2

NGC 2024-IRS2 is a bright infrared source in the NGC 2024 nebula, which is excited by the nearby source IRS2b (Bik et al. 2003). Deep VLA observations at 3.6 cm by Rodríguez, Gomez & Reipurth (2003, hereafter RGR03) detected both IRS2 and IRS2b, as well as a close companion to IRS2b. Alvarez et al. (2004) detect IRS2 as a point source with no evidence for secondary companions

or extended emission. IRS2 underwent an outburst between 1989 and 1991 whereby its near-infrared output increased by a factor of 2.5 (Nisini et al. 1994); IRS2 is also variable at radio wavelengths (Lenorzer et al. 2004).

IRS2 was imaged at all four wavelengths in our survey, and the results are shown in Fig. 4. IRS2 is unresolved at all wavelengths, with the possible exception of 43 GHz where the emission appears circularly-symmetric despite the elongated beam. The deconvolved source size indicates an elongated source along an axis perpendicular to the beam. Since IRS2 is our closest source our resolution at 43 GHz is probing ionized gas on scales of 17–20 AU from the central star. The flux we measure for IRS2 at 8.5 GHz (18.5 mJy) is
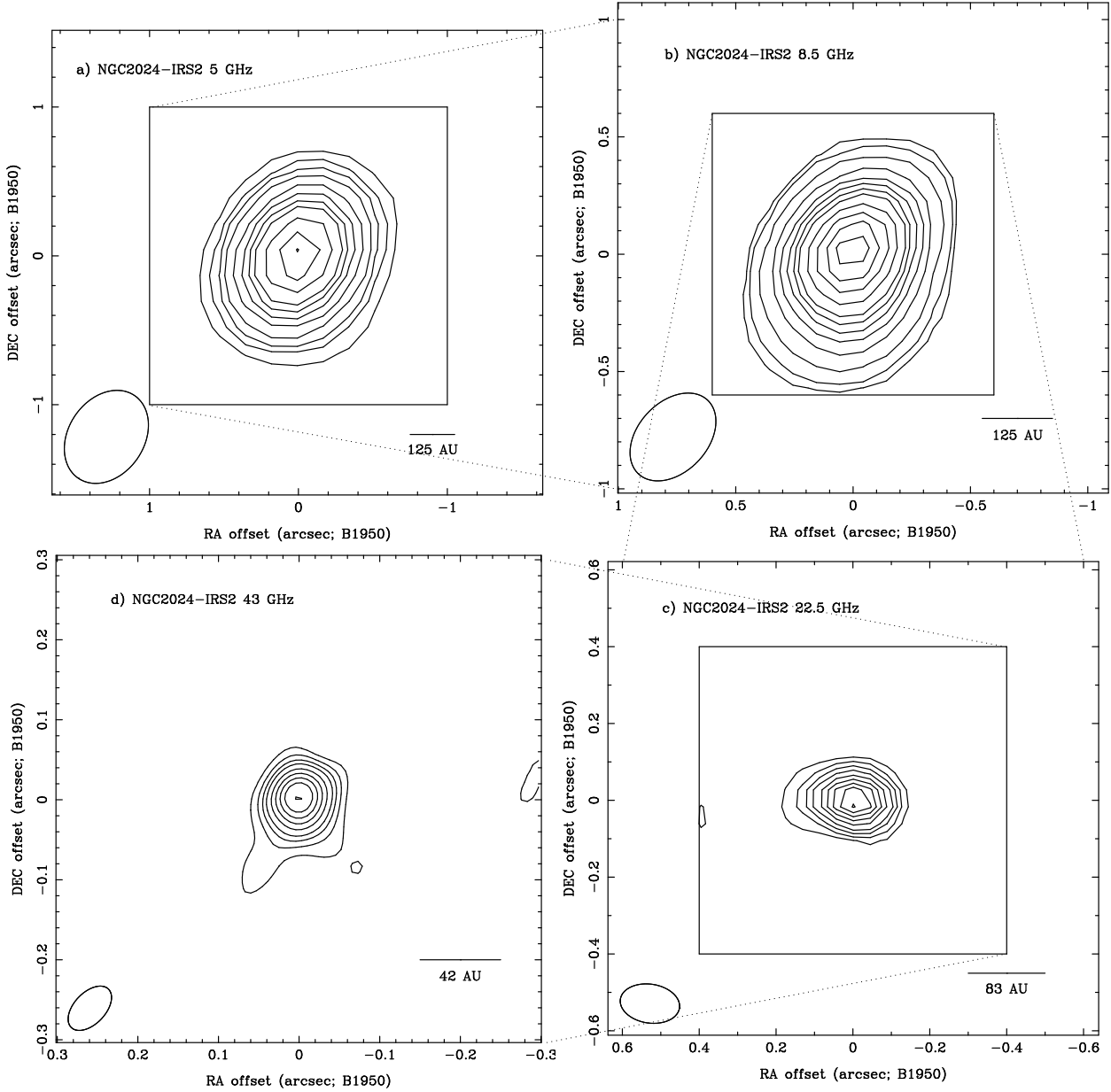
Figure 4. Images of NGC 2024-IRS2 at each frequency, clockwise starting from top left: a) 5 GHz, b) 8.5 GHz, c) 22.5 GHz and d) 43 GHz. Contours are at a) $-3, 3, 5, 7, 10, 15, 20, 25, 30, 40, 50, 60, 70 \times 0.20$ mJy beam^{-1}; b) $-3, 3, 5, 10, 20, 30, 40, 50, 60, 80, 100, 120, 140, 160 \times 0.091$ mJy beam^{-1}; c) $-3, 3, 5, 7, 9, 12, 15, 18, 21, 25, 30, 35, 40 \times 0.47$ mJy beam^{-1}; and d) $-3, 3, 5, 7, 9, 12, 15, 18, 21, 25, 30, 35, 40 \times 0.40$ mJy beam^{-1} respectively. The large box in a), b) and c) represents the size of the next image. The open ellipse in the bottom left corner represents the beam, and a scale bar is shown as a horizontal line assuming the distance given in Table 1. The NE extension on the 22.5-GHz image is a residual phase error.

in good agreement with the recent measurement of RGR03, which they note is approximately a factor of 2 higher than previous observations (Kurtz, Churchwell & Wood 1994). RGR03 also show that IRS2 is slightly extended to the east at 8.5 GHz, with perhaps a second source 0.37 arcsec ESE of IRS2 which we do not see in any of our images.

The radio spectrum for IRS2 rises only slowly across the range of frequencies observed here with a fitted spectral index of only $+0.18 \pm 0.08$. The spectrum appears to show some flattening above 8.5 GHz, giving rise to a spectrum closer that expected for an H II region. The value of the angular size power-law index, ζ, is lower than that expected for a uniform wind. The brightness temperature

of IRS2 increases slightly with frequency, decreasing again at 43 GHz, but the variation is small (see Table 5).

We do not detect either of the sources associated with IRS2b (VLA 15 and 16 in the notation of RGR03). For VLA 15 this is a sensitivity issue since its flux density at 8.5 GHz is only 0.24 mJy (RGR03) and would only be detected at the 3-σ level in our map. The non-detection of VLA 16 suggests that it may also be time-variable.

We note that our 22-GHz flux is lower than previous measurements. Lenorzer et al. (2004) suggest that IRS2 underwent a period of radio brightening in 1994-1995 relaxing to lower levels around 2002, a period for which they have no other data. Our data for
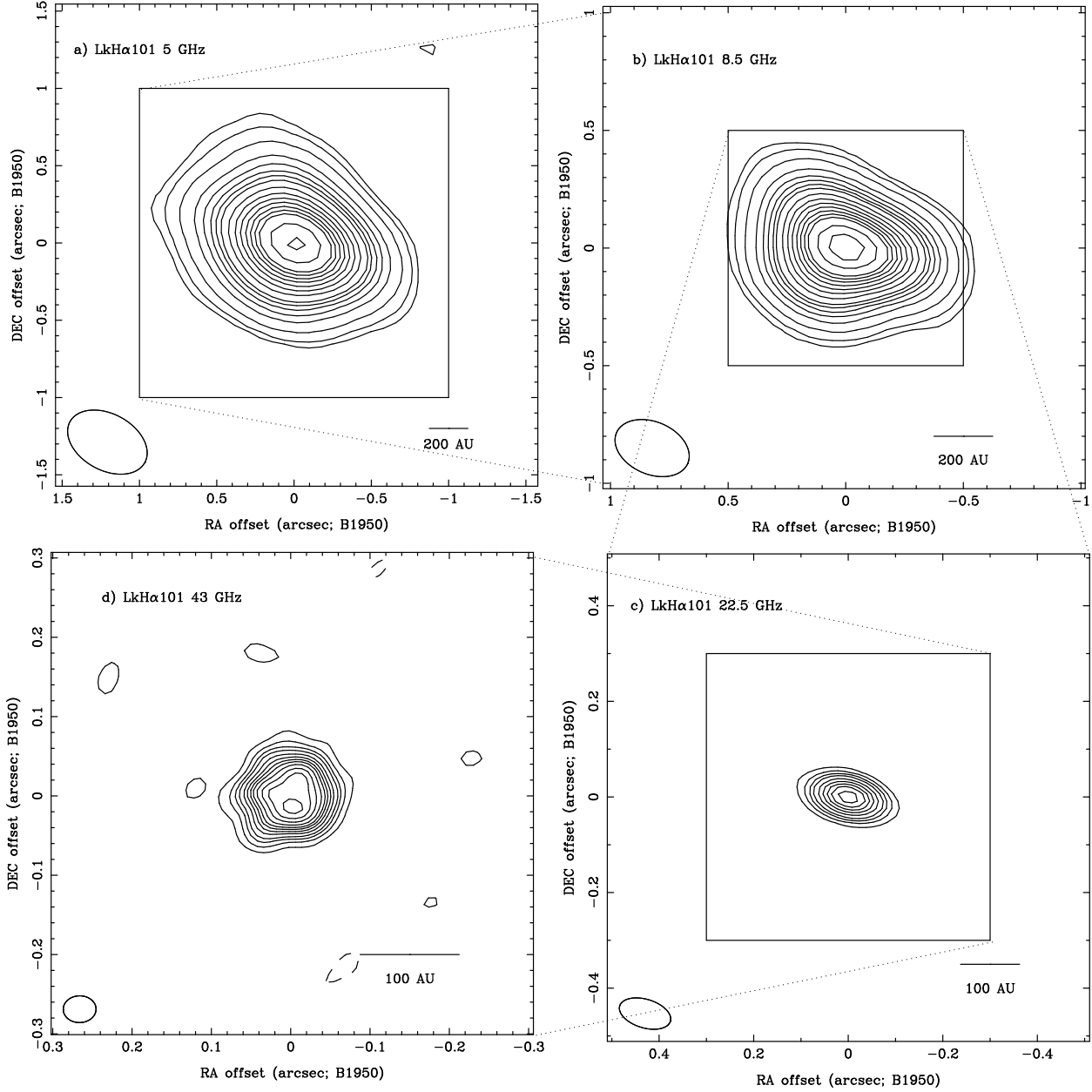
Figure 5. Images of LkHα101 at each frequency, clockwise starting from top left: a) 5 GHz, b) 8.5 GHz, c) 22.5 GHz and d) 43 GHz. Contours are at a) −3, 3, 5, 10, 20, 30, 40, 50, 60, 80, 100, 120, 140, 160, 180, 200, 250, 300×0.043 mJy beam^{-1} b) −3, 3, 5, 10, 20, 30, 40, 50, 60, 80, 100, 120, 140, 160, 180, 200, 250, 300, 350, 400, 450×0.055 mJy beam^{-1} c) −3, 3, 5, 10, 15, 20, 25, 30, 35, 40, 45, 50, 55, 60×0.30 mJy beam^{-1} and d) −3, 3, 5, 7, 9, 12, 15, 18, 21, 25, 30, 35×0.31 mJy beam^{-1} respectively. The large box in a), b) and c) represents the size of the next image. The open ellipse in the bottom left corner represents the beam, and a scale bar is shown as a horizontal line assuming the distance given in Table 1.

1996 November 1 show that NGC2024-IRS2 must have decreased in brightness rather more rapidly, reaching pre-outburst fluxes (at least at high frequencies where the gas will become optically thin first) within a period of 15 months. However, we have made the only 43-GHz measurement to date which makes it difficult to assess how much the flux at that frequency has changed. Lenorzer et al. (2004) model the radio spectrum pre- and post-outburst as a recombining stellar wind with modest differences (of order a factor of 2) in the outer radius and electron density at the stellar surface.

Bik et al. (2003) suggested that IRS2b is the exciting source of the NGC 2024 H II region. Comparing our results with RGR03 shows that the 8.5-GHz flux of IRS2b (VLA 16 in their terminol-

ogy) increased by a factor of at least 3 over the time period 1996 November to 2002 March. Kurtz et al. (1994) also did not detect it at 8.5 and 15 GHz to a 3σ level of 0.33 and 2.2 mJy respectively. Thus it may be that IRS2b is currently undergoing an outburst, and observations are clearly required to explore this further.

3.5 LkHα101

LkHα101 is a Herbig Be star at a distance of 700 pc (Herbig et al. 2004), associated with an optical reflection nebula (NGC 1579) and a compact H II region (S222). Previous VLA observations by Becker & White (1988) revealed a compact stellar-wind source

Table 5. Fluxes of radio sources detected. Peak ($F_{\rm pk}$) and total ($F_{\rm tot}$) flux densities are given in mJy beam^{-1} and mJy respectively. Brightness temperatures ($T_{\rm b}$) are derived from the peak flux and are quoted in K. Uncertainties in the brightness temperatures are derived from those for the corresponding flux density. The tenth column lists the derived spectral index. Upper limits are given as 3-σ where σ is taken from Table 4. The Notes column indicates if only 2 points have been used to derive the spectral index.

Source	ν GHz	$S_{\rm pk}$ mJy beam^{-1}	$S_{\rm tot}$ mJy	$T_{\rm b}$ K	α	Notes
S 106-IR	8.5	4.5±0.1	4.8±0.3	2060±45	0.65±0.11	VLA only
	22.5	7.9±0.2	10.7±0.4	2500±60		
	43	6.7±0.4	14.0±0.4	3530±210		
	23	3.6±1.0	12.1±2.0	12500±4000		MERLIN
S 140-IRS1	5	1.9±0.1	2.8±0.3	580±30	0.61±0.03	
	8.5	1.9±0.1	3.7±0.2	570±30		
	22.5	3.4±0.2	4.2±0.3	970±60		
	43	3.7±0.4	10.4±0.5	1850±200		
S 140-IRS2N	5	1.5±0.1	1.7±0.1	460±30	0.77	2
	8.5	2.4±0.1	2.6±0.3	720±30		
	22.5	<0.78	<0.78	–		
	43	<1.08	<1.08	–		
W75N-VLA1	5	1.4±0.1	1.7±0.1	450±30	−1.60	2
	8.5	0.7±0.1	0.7±0.1	220±30		
	22.5	<0.96	<0.96	–		
	43	<0.90	<0.90	–		
W75N-VLA3	5	0.7±0.1	0.9±0.1	220±30	0.79±0.15	
	8.5	1.6±0.1	2.0±0.1	490±30		
	22.5	3.5±0.4	3.7±0.5	1040±120		
	43	3.1±0.3	5.2±0.3	1560±150		
W75N-Bc	5	0.5±0.1	0.6±0.1	160±30	−0.34	2
	8.5	0.4±0.1	0.5±0.1	120±30		
	22.5	<0.96	<0.96	–		
	43	<0.90	<0.90	–		
NGC 2024-IRS2	5	12.1±0.2	13.8±0.1	1840±30	0.18±0.08	
	8.5	13.8±0.1	18.4±0.2	1850±15		
	22.5	17.0±0.4	22.0±0.5	2620±60		
	43	10.0±0.4	20.7±0.5	2500±100		
Lk Hα101	5	13.4±0.1	19.7±0.5	3450±25	0.51±0.06	
	8.5	18.5±0.1	30.0±0.6	4300±25		
	22.5	16.0±0.3	20.0±2.0	5800±109		
	43	13.1±0.3	62.4±2.5	6110±140		

within a more extended shell-like H II region. MERLIN observations by Hoare et al. (1994) and Hoare & Garrington (1995) at 5 and 1.6 GHz resolved structure in the stellar wind on scales of ∼50 AU, while Bieging, Cohen & Schwartz (1984) also noted departures from circular symmetry in their 5 and 15 GHz VLA images. Recently Alvarez et al. (2004) made near-infrared speckle observations of LkHα101 and detected a secondary component 0.17 arcsec to the east of the main star. Even higher resolution infrared observations by Tuthill et al. (2002) reveal both the secondary source and show that LkHα101 has a shell-like appearance in the 1–3 μm range, which they modelled as an almost face-on disc with a central hole.

LkHα101 was imaged at all four wavelengths in our survey, and the results are shown in Fig. 5. Since all our observations used only the VLA A configuration we are not sensitive to emission from the ionized gas on scales greater than 10 arcsec. In practice our images contain no emission on scales much larger than the beam itself: we only detect emission from the central ionized wind rather than the more extended H II region seen by Becker & White (1988).

LkHα101 is resolved at all wavelengths. The 5 and 8.5 GHz images (Figs 5a and b) show some asymmetry in the lower contours, and our 8.5 GHz image bears a strong resemblance to the 15 GHz image of Bieging et al. (1984). However we do not detect their SE extension in any of our images. Our 5-GHz data are in reasonable agreement with those of Becker & White (1988); the total flux in our image is only about two-thirds of their measurement (although our peak flux is in good agreement with the measurement of Bieging et al. 1984), probably due to our insensitivity to emission on larger scales.

The new result here comes from our 43 GHz data. The emission retains a high degree of circular symmetry, even on scales of less than 100 AU. We do not detect the secondary companion to the east. The plateau-like appearance in Fig. 5d is genuine and not an artefact of the choice of contour levels. Such an appearance is consistent with an equatorial wind viewed face on and the near face-on view proposed by Tuthill et al. (2002). We measure a total flux of 62 mJy at this frequency, somewhat less than expected based on extrapolating the observations of Becker & White (1988), although
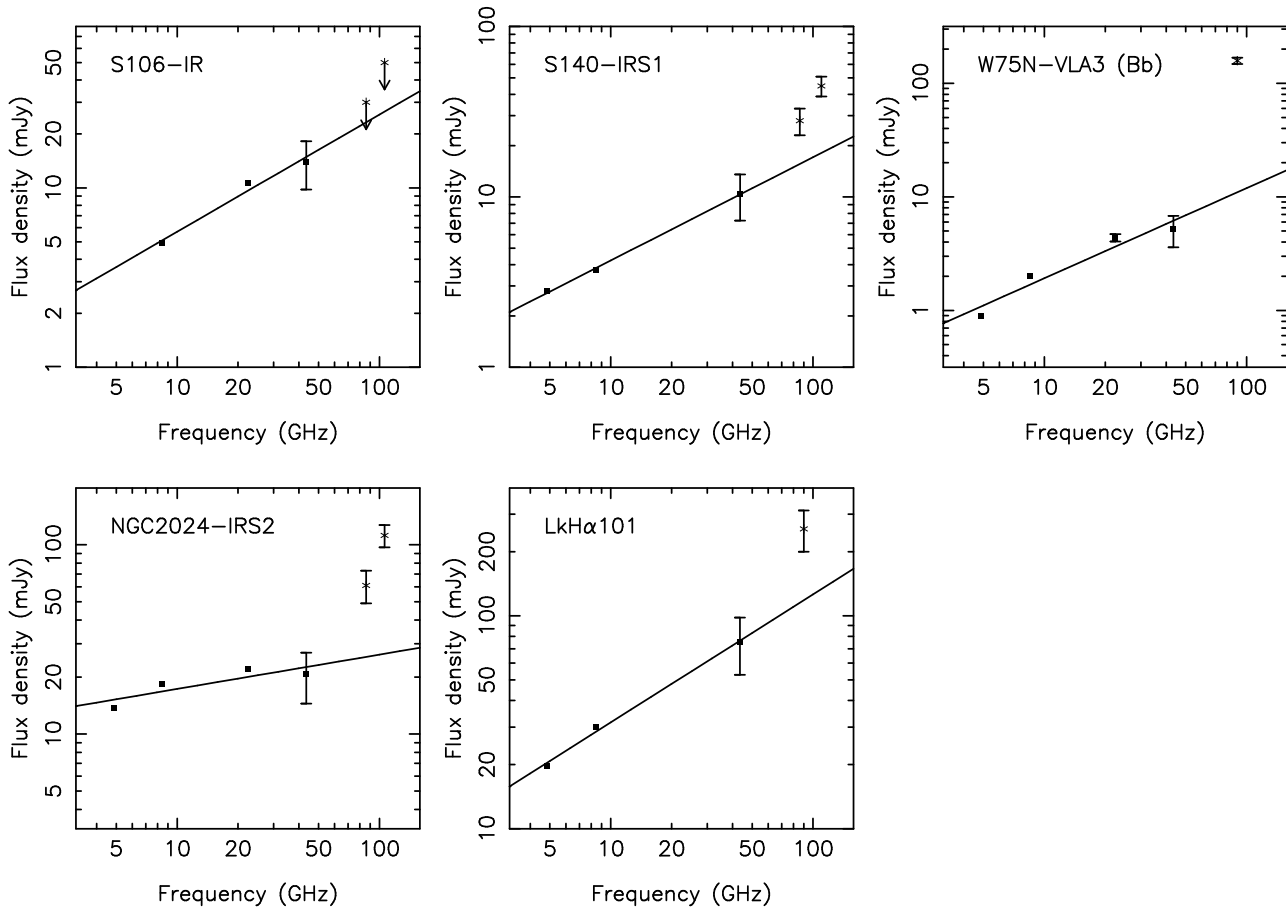
Figure 6. Radio spectral energy distributions for the sources in our sample (filled squares). Error bars are drawn where they are greater than the symbol size. The 22.5-GHz data points for LkHα101 and S140-IRS1 have been omitted as they appear to be significant underestimates of the flux density at this frequency. Asterisks mark 3-mm measurements, taken with much larger beams than the radio. For NGC 2024-IRS2 and S 106-IR (upper limits) these are our Plateau de Bure data at 86 and 106 GHz. For S140-IRS1 these are OVRO measurements at 86 and 110 GHz (Gibb, Hoare & Shepherd, in preparation). Points for W75N and LkHα101 are taken from Shepherd (2001) and Altenhoff, Thum & Wendker (1994) respectively.

we are probably only detecting the inner regions of the wind. However, we calculate a peak brightness temperature of ∼6000 K from our 43 GHz measurements, lower than expected if we were detecting emission from the innermost regions of the wind.

The spectral index for LkHα101 is 0.51±0.06 (excluding our 22.5-GHz data), is in agreement with the value expected for an ionized wind at the 2-σ level. If we apply a taper to the 43-GHz data (reducing the resolution to 0.2 arcsec) then we recover a total flux of ∼75-80 mJy, which then yields a spectral index of 0.61±0.04. Examining Fig. 6 shows that the 43 GHz point lies below a line extrapolated from the 5 and 8.5-GHz points. However, the A-array VLA data of Becker & White (1988) yield a 22.5-GHz flux density of order 60–80 mJy, which implies a 43-GHz flux density of more than 100 mJy assuming the above spectral index. The most likely explanation for our apparently anomalously low 22.5-GHz measurement is our poorer sensitivity. The brightness temperatures increase with frequency from 3450 to 6110 K, and are the highest of all our sources at each frequency. Despite that fact, they are still consistently below 10 000 K and the stellar effective temperature. This may be explained if the emission becomes optically thick in a relatively cool region of the wind, or the filling factor is less than 100 per cent.

The MERLIN observations of Hoare et al. (1994) show that the wind is resolved on scales of a few tens of AU at 5 GHz. The more circular appearance that we obtain at 43 GHz compared with the MERLIN 5-GHz image can be attributed to the emission being less well-resolved at 43 GHz. The angular size we derive at 43 GHz (74 milliarcsec) is in good agreement with that predicted from the MERLIN data, assuming that the size falls of as $\nu^{-0.6}$ (Wright & Barlow 1975). Therefore, the ionized gas towards LkHα101 appears to be well-characterized by a spherically-symmetric, constant velocity wind, a conclusion reinforced by the results of the modelling described in Section 4.2.

There are a number of possible reasons for lower-than-expected flux densities at the highest frequencies. One explanation which applies to the VLA (or any interferometer) in its most extended configuration operating at the highest frequencies is decorrelation due to phase noise, which leads to a reduction in the visibility amplitude on the longest baselines. However, plots of the calibrator visibility amplitudes showed that the fast-switching technique had successfully stopped the atmosphere and decorrelation was negligible. Another reason may be our absolute calibration at 43 GHz, since we assumed, rather than derived, a flux density for our primary calibrator. The most likely explanation is that we have
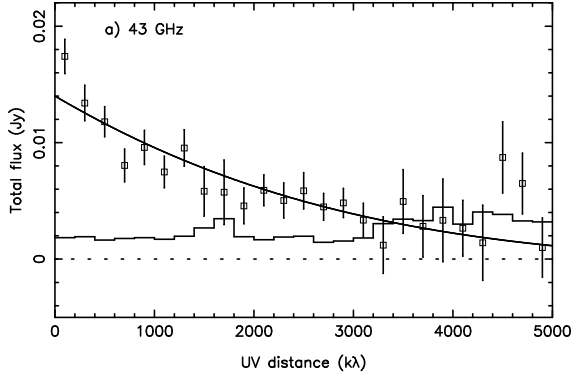
Figure 7. S106-IR visibility amplitude for 43 GHz data. The amplitude is in Jy and the baseline is in kilo-wavelengths. The error bars are ± 1-σ. The best-fitting model from Table 7 is also shown as a solid curve. The histogram in this and subsequent figures denotes the expected flux (due to noise alone) in the presence of zero signal.

resolved the wind at 43 GHz and the more extended emission is too weak to be detected by our observations. However poor sampling at short baselines can also result in a significant underestimate of the total flux (Wilner & Welch 1994).

4   MODELLING THE RADIO EMISSION AS A UNIFORM SPHERICAL WIND

4.1   Model description

In order to explore the nature of the ionized emission, we have followed the analysis of Becker & White (1982, hereafter BW82) and modelled the emission from a uniform temperature spherical stellar wind. As these authors argue, for stellar wind sources with extended faint emission it is better to analyze interferometer data in the spatial-frequency domain rather than the image domain. In their model, the only free parameters are the total flux (i.e. flux at zero baseline length, S_{T}) and the wind temperature (T_{w}). The slope of the visibility function constrains the wind temperature, while the extrapolated zero-spacing flux constrains the total flux or equivalently, $\dot{M}/v_{\infty}$, the mass-loss rate divided by the wind terminal velocity.

Table 7 lists the best-fitting parameters for each source. Table 8 lists a number of properties derived from the models, including $\dot{M}/v_{\infty}$ which we convert to a mass-loss rate assuming a wind terminal velocity where known (typically in the range 200–400 km s^{-1}: see, e.g. Drew et al. 1993; Chandler, Carlstrom & Scoville 1995; Bunn et al. 1995; Lenorzer et al. 2004). These mass-loss rates are not very sensitive to the adopted wind temperature but obviously scale directly with the wind velocity.

Figs 7 to 10 show plots of the azimuthally-averaged visibility amplitude as a function of baseline length for each source, with the best fitting spherical wind models overlaid. The error bars represent the 1-σ noise level and the histogram on each plot represents the expected flux for zero signal based on the noise level. When determining the goodness of fit, data points less than 1σ different from the zero-signal flux were excluded.

Good fits were obtained if the value of χ^2 passed through a well-defined minimum. In general the total fluxes were reasonably well-constrained, often exhibiting well-defined minima in the χ^2 distribution. Reasonable fits could typically be obtained with a wide range of temperatures (typically 2000 to 5000 K).
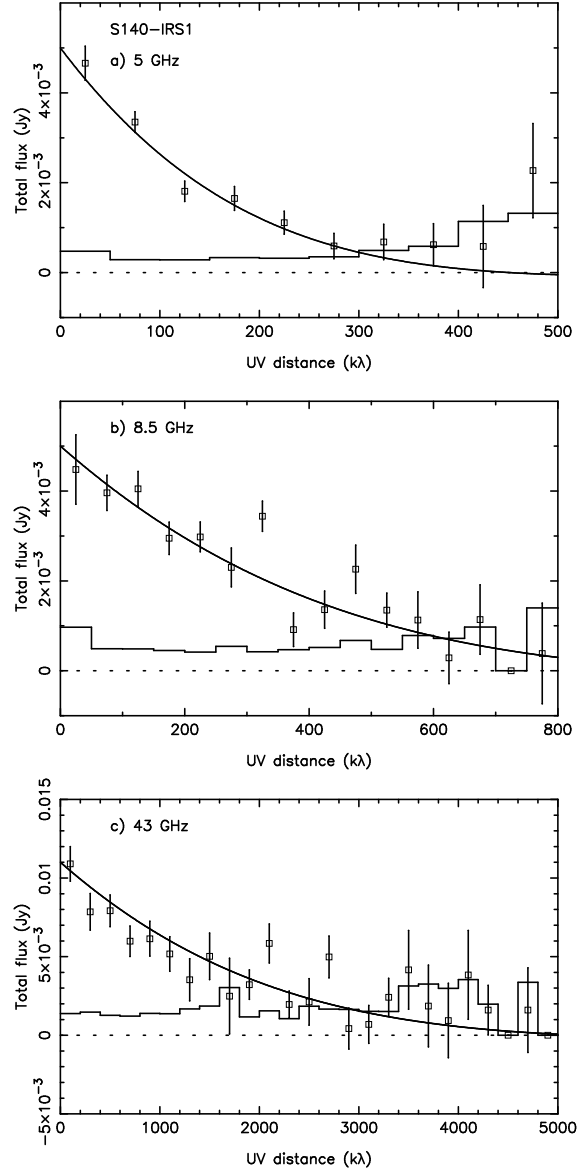

Figure 8. S140-IRS1 visibility amplitude for 5, 8.5 and 43 GHz. The amplitude is in Jy and the baseline is in kilo-wavelengths. The error bars are ± 1-σ. The best-fitting models from Table 7 is also shown as a solid curve.

The best-fitting flux at higher temperatures tended to be lower than that at lower temperatures. This is easy to understand. For a given flux density, at high temperatures the model visibility function falls off more slowly than at low temperatures. Thus in order to yield a 'good' minimum-χ^2 fit, the total flux must decrease.

4.2   Modelling results for each source

The main result from this modelling is that the fitted wind temperatures are low, typically 3000–4000 K, much less than the effective temperatures for main-sequence stars with the luminosities given in Table 1 (22 000 to 30 000 K). They are also much less than half the effective temperature, which has been shown to be an appropriate value for the wind temperature in main-sequence O stars (Drew 1989). However, they are not unprecedently low: Becker & White (1988) derived a temperature in the range 6800 to 7800 K for LkHα101, about 25 per cent higher than the values we derived.

Table 6. Observed and deconvolved sizes of radio sources at each detected wavelength. Columns 3–5 list the parameters derived from the fits while columns 6–8 list the parameters for a gaussian deconvolution. The angular size-frequency power law index, ζ, is listed in column 9. Two values are listed for each source: the first value is from a fit to the convolved (fitted) sizes, the second value is from a fit to the deconvolved sizes. The Notes column indicates if only 2 points have been used in the fit for ζ. In some cases the error in the deconvolved solution is as large as the minor axis.

Source	ν GHz	θ_a arcsec	θ_b arcsec	PA deg	θ_a' arcsec	θ_b' arcsec	PA deg	ζ	Notes
S 106-IR	8.5	0.25±0.02	0.18±0.02	153±4	0.04±0.04	0.02±0.02	150±30	−0.95±0.14	
	22.5	0.105±0.001	0.079±0.006	71±1	0.025±0.025	0.01±0.01	143±0	−0.45±0.24	
	43	0.049±0.009	0.034±0.003	107±3	0.031±0.010	0.010±0.009	129±28		
S 140-IRS1	5	0.60±0.01	0.42±0.01	169±1	0.35±0.02	0.11±0.05	34±2	−0.93±0.05	
	8.5	0.40±0.01	0.27±0.01	16±1	0.32±0.01	0.03±0.03	37±1	−0.69±0.27	
	22.5	0.122±0.009	0.077±0.006	169±6	0.033±0.014	0.025±0.025	27±40		
	43	0.081±0.007	0.048±0.004	70±6	0.074±0.006	0.026±0.007	66±4		
S 140-IRS2N	5	0.60±0.02	0.03±0.01	157±2	0.22±0.06	0.06±0.06	171±12	−0.95±0.14	2
	8.5	0.32±0.01	0.19±0.01	156±2	0.06±0.02	0.02±0.02	80±40	−0.45±0.04	2
W75N-VLA1	5	0.50±0.02	0.37±0.01	145±5	0.17±0.03	0.08±0.03	53±41	−1.11±0.02	2
	8.5	0.30±0.01	0.31±0.01	141±5	0.12±0.03	0.05±0.05	110±26	−0.97±0.21	2
W75N-VLA3	5	0.50±0.10	0.36±0.03	145±2	0.33±0.01	0.10±0.10	120±20	−1.05±0.08	
	8.5	0.32±0.01	0.20±0.01	144±2	0.13±0.01	0.06±0.01	141±2	−0.75±0.30	
	22.5	0.141±0.012	0.075±0.006	2±5	0.094±0.015	0.002±0.002	4±4		
	43	0.048±0.004	0.043±0.004	131±33	0.031±0.007	0.022±0.008	0±20		
W75n-Bc	5	0.67±0.07	0.41±0.04	138±8	0.43±0.08	0.24±0.01	131±18	−1.21±0.41	2
	8.5	0.30±0.03	0.27±0.02	116±41	0.20±0.20	0.03±0.03	67±13	−2.00±0.35	2
NGC 2024-IRS2	5	0.69±0.02	0.54±0.02	148±2	0.22±0.03	0.10±0.10	60±40	−1.00±0.07	
	8.5	0.44±0.02	0.33±0.03	143±7	0.23±0.23	0.11±0.11	17±17	−0.86±0.89	
	22.5	0.165±0.010	0.110±0.010	82±1	0.081±0.081	0.069±0.069	92±92		
	43	0.072±0.007	0.055±0.015	148±12	0.045±0.020	0.019±0.019	17±15		
Lk Hα101	5	0.640±0.002	0.470±0.001	64±14	0.330±0.003	0.290±0.002	84±2	−0.86±0.01	
	8.5	0.420±0.002	0.290±0.001	74±1	0.260±0.002	0.180±0.001	86±1	−0.68±0.02	
	22.5	0.121±0.002	0.065±0.001	76±1	0.047±0.001	0.024±0.001	86±6		
	43	0.085±0.003	0.075±0.002	115±11	0.074±0.005	0.066±0.002	122±13		

Table 7. Best-fitting spherically-symmetric, isothermal wind model parameters for each frequency. The total flux is in mJy and the wind temperature is in K. The final column gives the spectral index (α_{mod}) corresponding to the best-fitting fluxes at each frequency.

Source	5 GHz		8.5 GHz		22.5 GHz		43 GHz		α_{mod}
	S_T	T_w	S_T	T_w	S_T	T_w	S_T	T_w	
S106-IR	–	–	–	–	–	–	14.0±1.0	5000±1000	—
S140-IRS1	$5.0^{+0.5}_{-1.5}$	500^{+1500}_{-500}	5.0±1.0	1000^{+2000}_{-500}	–	–	10.0±2.0	2000^{+2000}_{-500}	0.35±0.15
NGC 2024-IRS2	14.0±2.0	3000±1000	20.0±3.0	4000±1000	24.0±3.0	4000±1000	26.0±3.0	3000±1000	0.27±0.07
LkHα101	14.5±1.5	5000±1000	25.0±2.0	5000±1000	35.0±5.0	4500±1500	58.0±2.0	4000^{+1500}_{-500}	0.59±0.08

For LkHα101 the solutions at 22.5 and 43 GHz have wind temperatures which are lower than the observed brightness temperatures at these frequencies. However, given the absolute calibration uncertainty at these frequencies (see Section 2) this discrepancy is probably not significant. LkHα101 was quite well-fitted by a uniform, isothermal spherical wind at all frequencies, as was NGC 2024-IRS2. Reasonably good fits were obtained for S106-IR and S140-IRS1 at 43 GHz, but W75N-VLA3 was not well fitted at any frequency. We now discuss the results for each source in turn.

S106-IR: The 8.5 and 22.5-GHz data could not be fitted with any temperature. At 43 GHz the fit was quite well-constrained in total flux of 14 mJy for temperatures in the range 4000 to 6000 K.

S140-IRS1: At 5 GHz the best fitting flux was 5 mJy for a temperature of 500 K. Reasonable fits were possible in the range 3.5 to 5.5 mJy and temperatures between 500 and 2000 K. At 8.5

GHz the best fit occurred at 1000 K, also for a total flux of 5 mJy. As with S106-IR, no fits were possible at 22.5 GHz. At 43 GHz the total flux was constrained to be ∼10 mJy. The temperature was less well constrained and reasonable fits in the range 1500 to 4000 K were possible.

NGC2024-IRS2: At 5 GHz the flux was quite well-constrained at 14 mJy. The corresponding temperatures were in the range 2000 to 4000 K. The fits at 8.5 GHz were moderately-well constrained with a best-fitting flux of 20 mJy and temperatures of 3000 to 5000 K. Fits were possible at 22.5 GHz although they were relatively poorly constrained with in the range 20–27 mJy for temperatures between 3000 and 5000 K. At 43 GHz the best-fitting flux was ∼26 mJy for temperatures between 2000 and 4000 K.

LkHα101: The best-constrained fits were obtained for the brightest source, LkHα101. At 5 GHz the best-fit flux was 14.5

Table 8. Properties derived from the best-fitting wind models listed in Table 7 for each frequency. The notation $a(b)$ denotes $a \times 10^b$.

Source	ν GHz	$\dot{M}/v_\infty$ $M_\odot\,\mathrm{yr}^{-1}\,(\mathrm{km\,s}^{-1})^{-1}$	q_1 AU	θ_1 arcsec	η_{ff}	$\dot{M}$ $M_\odot\,\mathrm{yr}^{-1}$
S106-IR	43	$5.2\pm0.4\times10^{-9}$	$9.8^{+1.5}_{-1.2}$	$0.016^{+0.003}_{-0.002}$	$0.21^{+0.05}_{-0.06}$	1.8×10^{-6}
S140-IRS1	5	$1.4^{+0.2}_{-0.4}\times10^{-8}$	239^{+11}_{-139}	$0.26^{+0.02}_{-0.15}$	$0.40^{+0.06}_{-0.33}$	4.2×10^{-6}
	8.5	$1.0\pm0.2\times10^{-8}$	100^{+54}_{-48}	$0.11^{+0.06}_{-0.05}$	$0.21^{+0.29}_{-0.15}$	3.0×10^{-6}
	43	$8.0^{+1.4}_{-1.6}\times10^{-9}$	$19.7^{+5.2}_{-7.3}$	$0.022^{+0.005}_{-0.008}$	$0.37^{+0.19}_{-0.22}$	2.4×10^{-6}
NGC 2024-IRS2	5	$8.4\pm1.1\times10^{-9}$	76^{+24}_{-15}	$0.18^{+0.06}_{-0.04}$	$0.09^{+0.07}_{-0.04}$	$1.7–3.4\times10^{-6}$
	8.5	$8.4^{+1.2}_{-1.1}\times10^{-9}$	$46.4^{+11.1}_{-8.1}$	$0.11^{+0.03}_{-0.02}$	$0.09^{+0.06}_{-0.03}$	$1.7–3.4\times10^{-6}$
	22.5	$6.2\pm0.7\times10^{-9}$	$19.2^{+4.3}_{-3.2}$	$0.046^{+0.010}_{-0.008}$	$0.15^{+0.07}_{-0.05}$	$1.2–2.4\times10^{-6}$
	43	$5.1\pm0.6\times10^{-9}$	$12.1^{+3.5}_{-2.3}$	$0.029^{+0.008}_{-0.006}$	$0.34^{+0.21}_{-0.13}$	$1.0–2.0\times10^{-6}$
LkHα101	5	$2.2\pm0.2\times10^{-8}$	115^{+20}_{-16}	$0.14^{+0.03}_{-0.02}$	$0.10^{+0.05}_{-0.03}$	6.6×10^{-6}
	8.5	$2.6\pm0.2\times10^{-8}$	$88.4^{+12.8}_{-8.3}$	$0.11^{+0.02}_{-0.01}$	$0.17^{+0.07}_{-0.03}$	7.8×10^{-6}
	22.5	$2.2\pm0.3\times10^{-8}$	$41.7^{+12.8}_{-8.3}$	$0.052^{+0.016}_{-0.010}$	$0.30^{+0.22}_{-0.11}$	6.6×10^{-6}
	43	$2.4\pm0.1\times10^{-8}$	$29.8^{+2.5}_{-4.8}$	$0.037^{+0.003}_{-0.006}$	$0.98^{+0.17}_{-0.29}$	7.2×10^{-6}

mJy with a temperature around 5000 K, although temperatures up to 8000 K gave reasonable fits. The 8.5-GHz fit showed a similar behaviour with a flux of 25 mJy and similar temperatures to 5 GHz. The fit at 22.5 GHz was not as well-constrained in flux (30–40 mJy) but quite well fitted with a temperature of 4500 K (plus or minus 1500 K). At 43 GHz the flux was not especially well-constrained with best-fit values in the range 56–60 mJy. The wind temperature was ∼4000 K, although temperatures up to 5500 K were almost as good.

W75N-VLA3: This source was too faint to be fitted at any wavelength for any temperature.

4.3   Lower-than-expected temperatures: clumpy winds?

As noted above, the model wind temperatures (Table 7) and the observed brightness temperatures (Table 5) are considerably lower than the values that might be expected for stars of these luminosities. Unlike Becker & White (1988), we see no trend for higher fitted temperatures at higher frequencies, despite the tendency in the observed brightness temperature estimates (Table 5). The uncertainties in the best-fitting model temperature do not rule out such a relation, however.

The emission from the model wind of BW82 is dominated by an optically thick core whose size varies with frequency. If the filling factor for this optically thick core is less than unity the true brightness temperature will be underestimated. From equation 5 of BW82 we can estimate the angular radius at which the wind emission becomes optically thick for each source. These values were calculated for each frequency for which we obtained a reasonable model fit, and are listed in Table 8. Comparing these values with the angular sizes derived in Table 6 shows that in many cases our observations are probing the regime where the wind becomes optically thick. The corresponding filling factors ($\eta_{\mathrm{ff}} = \theta_1^2/\theta^2$, where θ_1 is the angular diameter of the $\tau = 1$ surface given in Table 7 and θ is the geometric mean of the beam major and minor axes in Table 4) are in the range 0.2 to unity at 43 GHz implying that the observed brightness temperatures at that frequency tend to underestimate the actual gas temperatures. At lower frequencies η_{ff} tends to be much less than one. For LkHα101 the model yields wind temperatures which are in reasonable agreement in the range 6100 to 7500 K, reinforcing the conclusion that this source is well-modelled

by a spherical isothermal wind. The agreement between the wind temperature estimates at each frequency is poorer for all the other sources. In reality, the stellar wind is unlikely to be smooth as assumed by the modelling and thus the low filling factors are attained by the presence of clumps in the flow.

The appearance of S106-IR and S140-IRS1 (Figs 1 and 2 respectively) suggests that the wind is not spherically symmetric. Clearly such a wind would not completely fill the telescope beam and it is possible that a non-spherical geometry could mimic a lower-temperature spherical flow but this requires more detailed 2-D modelling and is beyond the scope of this paper.

Finally, two points related to interferometers are worth mentioning here. Decorrelation of the signal on long baselines reduces the measured flux, which might lead us to underestimate the temperature in our models. Decorrelation affects high frequency observations the most, which would show up as lower-than-expected temperatures at high frequencies. No such effect is seen in our observations, and there is no evidence for significant decorrelation in our data. The other point to note is that if we are missing extended flux, its recovery will not lead to higher-temperature fits: higher temperatures can only be obtained from the modelling if we are underestimating the flux on the *smallest* scales.

5   DISCUSSION: RADIO EMISSION FROM MASSIVE YSOS

Together the high frequency observations show that the rising thermal spectrum continues to 43 GHz in these massive YSOs. There is no evidence of the need for a dust contribution to the 43 GHz flux. For the sources with 90–110 GHz measurements there is a significant dust contribution at these higher frequencies. Even here this can disappear at high resolution when the flux at these frequencies can also be dominated by just the ionized wind (Plambeck et al. 1995; Gibb et al. 2004).

The origin of the +0.6 spectral index is a consequence of the contribution of both optically thin and thick emission (Wright & Barlow 1975; Panagia & Felli 1975). Schmid-Burgk (1982) showed that even non-symmetric winds will have a spectral index similar to the spherical case provided the electron density falls off as an inverse-square law. Finite (i.e. ionization-bounded) winds will show higher indices as the emission takes on the appearance of an
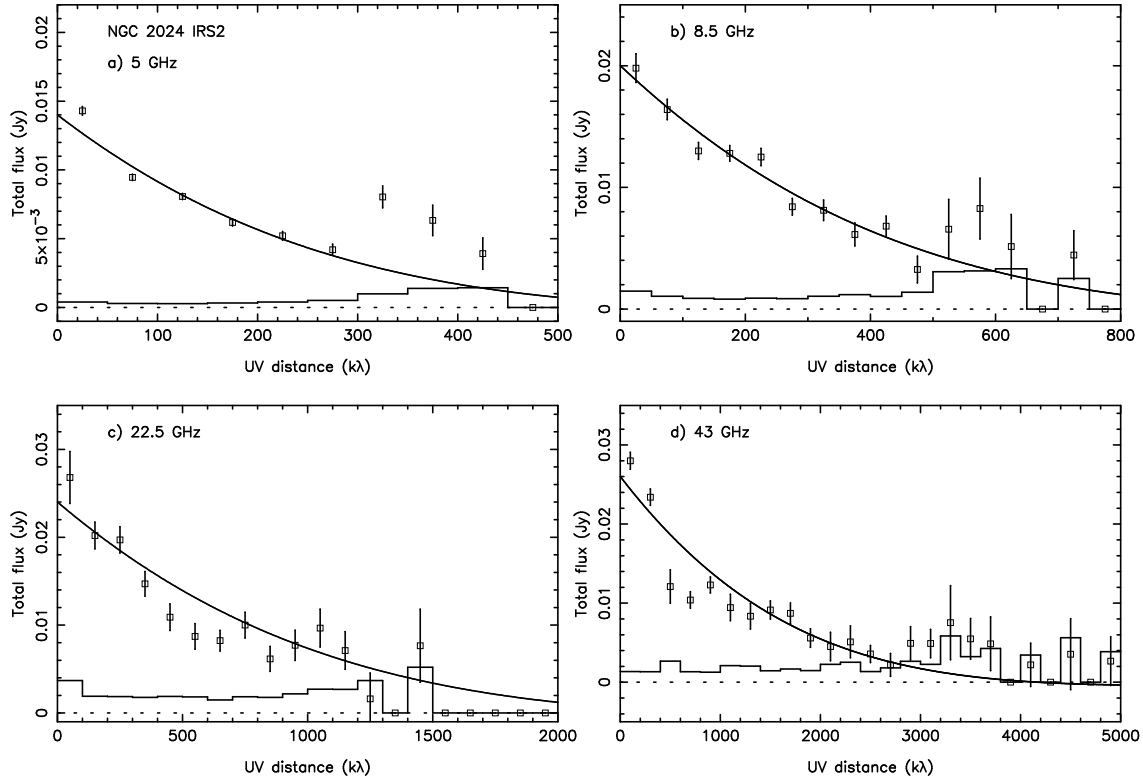
Figure 9. NGC2024 IRS2 visibility amplitude for each observed wavelength. The amplitude is in Jy and the baseline is in kilo-wavelengths. The error bars are ± 1-σ. The best-fitting model from Table 7 is also shown as a solid curve.
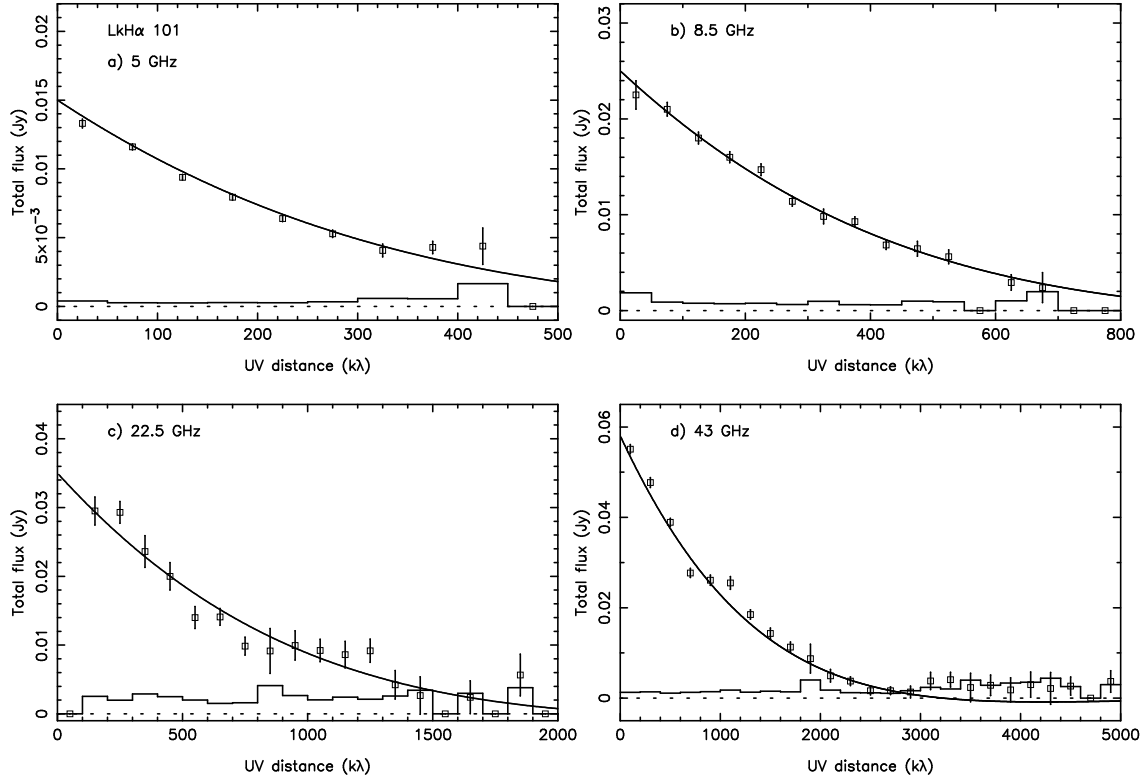

Figure 10. LkHα101 visibility amplitude for each observed wavelength. The amplitude is in Jy and the baseline is in kilo-wavelengths. The error bars are ± 1-σ. The best-fitting model from Table 7 is also shown as a solid curve.

optically thick H II region (Simon et al. 1983). Jets can have lower or higher values depending on the properties (Reynolds 1986), though detailed calculations of collimated winds lean towards values between +0.6 and +1, depending on the gradient in the electron density (Martin 1996). Models of photo-evaporating discs by Kessel, Yorke & Richling (1998) also predict spectral indices close to that expected for a spherical ionized wind, irrespective of inclination. Recently, Lugo, Lizano & Garay (2006) fitted the centimetre-wave spectrum of NGC 7538-IRS1 and MWC349A with a photo-evaporating disc model.

Within the uncertainties in our spectral index calculations, the winds from four of the five sources are consistent with constant velocity spherical flows. The spectral index for W75N-VLA3 is slightly larger and suggests that the wind may be recombining and/or accelerating. The spectral indices are also not consistent with the winds being collimated into bipolar jets. However, the values predicted by Reynolds (1986) are for an unresolved source; since we are resolving the emission, we are more likely to be dominated by the 'core' in his model which has a spherical-wind geometry.

Since we *are* resolving the wind, this does raise the question of the validity of the calculated spectral indices since the beams at different frequencies will be sampling different volumes of ionized gas. Naïvely it might be expected that the effect of this would be to artificially flatten the spectrum, thus implying that the spectral indices are lower limits. However, the modelling of the visibility data mitigates the usual problem of matching beams since the fitted flux is extrapolated to a zero-length baseline. Despite the large uncertainties, the model spectral indices are all consistent with ionized winds.

43 GHz observations of massive YSOs are also presented by Menten and van der Tak (2004) (CRL 2136), van der Tak and Menten (2005) (W33A, GL 2591, NGC 7538-IRS9), van der Tak et al. (2005) (W3-IRS5) and Reid et al. (2007) (Orion-I). The former find lower brightness temperatures and their C array fluxes and sizes are larger than their A array ones. This is ascribed to a centrally-peaked brightness distribution which is expected for a stellar wind and motivated our visibility-fitting approach. The sources in W3-IRS5 are mostly unresolved, but similar in flux and size to those presented here. They possibly resolve the 43 GHz emission from CRL 2136 and NGC 7538-IRS9 and the derived position angle of the elongation would align with the bipolar CO flow and therefore be jet-like. A similar alignment is seen in their C array data on GL 2591, consistent with the observation of a jet at 22 GHz by Trinidad et al. (2003), although intriguingly the higher resolution data has a different orientation and perhaps origin.

The main 43 GHz source observed in W33A is marginally extended in the C array data and possibly in the higher resolution A array data, although the derived position angles are very different, rather like GL 2591. For W33A there is no well-characterised bipolar CO flow, but 2MASS and Spitzer GLIMPSE images clearly show a large monopolar nebula extending to the SE, which likely has an outflow origin. The C array 43 GHz emission aligns with this within the uncertainties of the position angle and hence, may be a jet-like ionized flow. Furthermore, the interferometric observations of the 106 GHz and 233 GHz continuum emission from W33A-MM1 by van der Tak et al. (2000) appear to be elongated with a position angle of about 50–60 degrees. This is similar to that for the 43-GHz A array result. It is therefore interesting to speculate whether in this source (and possibly GL 2591) that a jet-like wind dominates the flux and morphology at the lower resolution and a dust disk or torus perpendicular to the wind is taking over at higher

resolution. The SED at high resolution indicates that this is indeed where the contributions of wind and dust are comparable.

van der Tak and Menten (2005) chose to interpret their 43 GHz data in terms of the gravitationally trapped H II region picture of Keto (2002). However, the sizes and fluxes are similar to those presented here and consistent with a stellar wind interpretation. The spectral indices of around unity can also be accommodated in a recombining wind picture. W33A and other sources with similar spectral indices such as GL 490 (Campbell et al. 1986) are also observed to have very broad (few 100 km s^{-1}) near-IR H I emission lines which again are consistent with a stellar wind interpretation (Bunn et al. 1995). Although the modelling of such winds in terms of geometry and assumptions still has some way to go to match all the observational data (e.g Höflich & Wehrse 1987; Sim et al. 2005), it is clear that a common origin for the IR line and radio continuum emission is very likely.

Another motivation for van der Tak and Menten (2005) to consider the gravitationally trapped H II region picture was to try and account for the lack of a strong, bright UCHII region powered by Lyman continuum radiation from these luminous sources. However, a stellar wind can also help here by reprocessing the hard radiation in the dense regions close to the star. For the mass-loss rates required to explain the radio emission it is predicted that the stellar wind would recombine (Höflich & Wehrse 1987) and hence very little Lyman continuum radiation would emerge into the surroundings. This also explains the spectral indices somewhat steeper than +0.6 that are often found (Moran et al. 1983). Such models would be a much better fit to the radio spectra found by van der Tak and Menten than the H II region models they present. To be effective in suppressing the ionizing continuum the wind would have to cover all directions. This does not seem feasible when these sources also power bipolar outflows that are also likely to originate from close to the star/inner disc. An alternative explanation is that ongoing accretion keeps the star in a swollen, low surface gravity, low effective temperature state during this phase (see discussion by Hoare & Franco 2007).

Finally we note the recent 43 GHz observations of Orion-I by Reid et al. (2007) which revealed an equatorial geometry for the wind. In their case the geometry is unambiguous as the SiO maser emission defines the outflow direction. They did not consider a wind origin for this emission and interpreted their data in terms of an ionized accretion disk instead. It is interesting to note the geometry of the 43-GHz emission from Orion-I is remarkably similar to that of S 140-IRS1, showing a twist or 'kink' in the contours (Fig. 2).

6   CONCLUSION

We have presented high-resolution observations made with the VLA in its A configuration at frequencies between 5 and 43 GHz of a sample of five massive young stellar objects (YSOs). The resolution varied from 0.04 arcsec (at 43 GHz) to 0.5 arcsec (at 5 GHz), corresponding to a linear resolution between 17 and 85 AU.

We resolved elongated emission at 43 GHz in S106-IR and S140-IRS1 confirming the equatorial wind nature of the emission from these two sources. This is further emphasized by a MERLIN 23-GHz observation of S106-IR which reveals a 44×18 AU^2 size for the radio source perpendicular to the large-scale outflow. The other sources were also partially resolved but were more difficult to relate to any bipolar outflow activity due to either being too evolved or within too complex an environment.

The spectral indices we derived are consistent with those for ionized stellar winds, not H II regions, with values ranging from +0.2 to +0.7. The sizes of the sources also scaled with frequency as expected for a stellar wind. We applied the procedure developed by Becker & White (1982) and directly model the visibility data in terms of an isothermal, spherical wind. Reasonable fits were obtained for some of the data. The derived wind temperatures of 3000–6000 K are somewhat lower than would be expected if the wind is heated by a main sequence star. If the wind is heated mostly by an accretion disc or by a low effective temperature star swollen by ongoing accretion this could explain the low wind temperatures. The observed brightness temperatures were also much lower than 10 000 K and indicated that there is likely to be significant beam dilution so the wind may also be clumpy or mixtures of optically thick and thin gas within the beam.

Further studies are needed to make use of the increased sensitivity, resolution and spatial frequency coverage of the VLA, to probe the ionized gas as close to the YSO as possible. However, in order to maintain sensitivity to larger spatial scales, it is important to obtain long (i.e. non-snapshot) tracks in multiple configurations, and at multiple wavelengths so that a more accurate picture can be derived for the ionized gas on circumstellar scales up to the size of molecular outflows. More sophisticated non-spherical models of the radio emission from equatorial winds and jets with temperature structure will be needed to compare with such data.

REFERENCES

Altenhoff W.J., Thum C., Wendker H.J., 1994, A&A, 281, 161
Alvarez C., Hoare M.G., Glindemann A., Richichi A., 2004, A&A, 427, 505
Bally J., Snell R.L., Predmore R., 1983, ApJ, ApJ, 272, 154
Bally J., Yu K.C., Rayner J., Zinnecker H., 1998, AJ, 116, 1868
Becker R.H., White R.L., 1982, ApJ, 262, 657
Becker R.H., White R.L., 1988, ApJ, 324, 893
Bieging J.H., 1984, ApJ, 286, 591
Bieging J.H., Cohen M., Schwartz P.R., 1984, ApJ, 282, 699
Bik A., Lenorzer A., Kaper L., Comerón F., Waters L.B.F.M., de Koter A., Hanson M.M., 2003, A&A, 404, 249
Bunn J.C., Hoare M.G., Drew J.E., 1995, MNRAS, 272, 346
Burrows C.J., Stapelfeldt K.R., Watson A.M., Krist J.E., Ballester G.E., Clarke J.T., Crisp D., Gallagher J.S., III, et al. 1996, ApJ, 473, 437
Carilli C., Holdaway M.A., 1999, Rad Sci, 34, 817
Chandler C.J., Carlstrom J.E., Scoville N.Z., 1995, ApJ, 446, 793
Davis C.J., Moriarty-Schieven G.H., Eislöffel J., Hoare M.G., Ray T.P., 1998, AJ, 115, 1118
Drew J.E., 1989, ApJS, 71, 267
Drew J.E., Bunn J.C., Hoare M.G., 1993, MNRAS, 265, 12
Drew J.E., Proga D., Stone J.M., 1998, MNRAS, 296, L6
Felli M., Simon M., Fischer J., Hamann F., 1985, A&A, 145, 305
Giardino G., Favata F., Micela G., 2004, A&A, 424, 965

Gibb A.G., Hoare M.G., Little L.T., Wright M.C.H., 2003, MNRAS, 339, 1011
Gibb A.G., Hoare M.G., Mundy L.G., Wyrowski F., 2004, in Burton M.G., Jayawardhana R., & Bourke T.L., eds, IAU Symposium 221: Star Formation at High Angular Resolution. Astron. Soc. Pac., San Francisco, p. 425
Herbig G.H., Andrews S.M., Dahm S.E., 2004, AJ, 128, 1233
Hoare M.G., 2002, in Crowther P.A., ed., The Earliest Phases of Massive Star Birth. Astron. Soc. Pac., San Francisco, p. 137
Hoare M.G., 2006, ApJ, 649, 856
Hoare M.G., Drew J.E., Muxlow T.B., Davis R.J., 1994, ApJ, 421, L51
Hoare M.G., Franco J., 2007, in Hartquist T.W., Falle S.A.E., Pittard J.M., Diffuse Matter from Star Forming Regions to Active Galaxies – A Volume Honouring John Dyson. Springer, Dordrecht, p. 61
Hoare M.G., Garrington S.T., 1995, ApJ, 449, 874
Hoare M.G., Glindemann A., Richichi A., 1996, in Käufl H.U., Siebenmorgen R., eds., The Role of Dust in the Formation of Stars. Springer Verlag, Berlin, p. 35
Hoare M.G., Muxlow T.B., 1996, in Taylor A.R., Paredes J.M., eds., Radio Emission from the Stars and the Sun. Astron. Soc. Pacific, San Francisco, p. 47
Höflich P., Wehrse R., 1987, A&A, 185, 107
Hunter T.R., Taylor G.B., Felli M., Tofani G., 1994, A&A, 284, 215
Keto E., 2003, ApJ, 599, 1206
Kurtz S.E., Churchwell E., Wood D.O.S., 1994, ApJS, 91, 659
Lenorzer A., Bik A., de Koter A., Kurtz S.E., Waters L.B.F.M., Kaper L., Jones C.E., Geballe T.R., 2004, A&A, 414, 245
Martí J., Rodríguez L.F., Reipurth B., 1993, ApJ, 416, 208
Martin S.C., 1996, ApJ, 473, 1051
Menten K.M., van der Tak F.F.S., 2004, A&A, 414, 289
Minchin N.R., Ward-Thompson D., White G.J., 1993a, A&A, 298, 894
Minchin N.R., White G.J., Padman R., 1993b, A&A, 277, 595
Moran J.M., Garay G., Reid M.J., Genzel R., Wright M.C.H., Plambeck R.L., 1983, ApJ, 271, L31
Nisini B., Smith H.A., Fischer J., Geballe T.R., 1994, A&A, 290, 463
Ouyed R., Clarke D.A., Pudritz R., 2003, ApJ, 582, 292
Panagia N., Felli M., 1975, A&A, 39, 1
Reipurth B., Heathcote S., Morse J., Hartigan P., Bally J., 2002, AJ, 123, 362
Reid M.J., Menten K.M., Greenhill L.J., Chandler C.J., 2007, ApJ, accepted (arXiv:astro-ph/0704.2309)
Reynolds S.P., 1986, ApJ, 304, 713
Richling S., Yorke H.W., 1997, A&A, 327, 317
Rodríguez L.F., Garay G., Curiel S., Ramírez S., Torrelles J.M., Gómez Y., Velázquez A., 1994, ApJ, 430, L65
Rodríguez L.F., Gómez Y., Reipurth B., 2003, ApJ, 598, 1100
Rodríguez L.F., Paveda A., Lizano S., Allen C., 2005, ApJ, 637, L65
Sault R.J., Teuben P.J., Wright M.C.H., 1995, in Shaw R.A., Payne H.E., Hayes J.J.E., eds., Astronomical Data Analysis Software and Systems IV. Astron. Soc. Pacific, San Francisco, p. 433
Schertl D., Balega Y., Hannemann T., Hofmann K.-H, Preibisch T., Weigelt G., 2000, A&A, 361, L29
Schmid-Burgk J., 1982, A&A, 108, 169
Schwartz P.R., 1989, ApJ, 338, L25
Shepherd D.S., 2001, ApJ, 546, 345
Shepherd D.S., Testi L., Stark D.P., 2003, ApJ, 584, 882
Shepherd D.S., Kurtz S.E., Testi L., 2004, ApJ, 601, 952
Sim S.A., Drew J.E., Long K.S., 2005, MNRAS, 363, 615
Simon M., Felli M., Cassar L., Fischer J., Massi M., 1983, ApJ, 266, 623
Smith N., Jones T.J., Gehrz R.D., Klebe D., Creech-Eakman M.J., 2001, AJ, 121, 984
Tofani G., Felli M., Taylor G.B., Hunter T.R., 1995, A&AS, 112, 299
Torrelles J.M., Gómez J.F., Rodríguez L.F., Ho P.T.P., Curiel S., Vázquez R., 1997, ApJ, 489, 744
Trinidad M.A., Curiel S., Cantó J., D'Alessio P., Rodríguez L.F., Torrelles J.M., Gómez J.F., Patel N., Ho P.T.P., 2003, ApJ, 589, 386
Tuthill P.G., Monnier J.D., Danchi W.C., Hale D.D.S., Townes C.H., 2002, ApJ, 577, 826

van der Tak F.F.S., Menten K.M., 2005, A&A, 437, 947

van der Tak F.F.S., Tuthill P.G., Danchi W.C., 2005, A&A, 431, 993

van der Tak F.F.S., van Dishoeck E.F., Evans N.J., II, Blake G.A., 2000,
    ApJ, 537, 283

Wilner D.J., Welch W.J., 1994, ApJ, 427, 898

Wilner D.J., Reid M.J., Menten K.M., 1999, ApJ, 513, 775

Wright A.E., Barlow M.J., 1975, MNRAS, 170, 41

This paper has been typeset from a TEX/ LATEX file prepared by the author.